Gondwana Research 125 (2024) 91–109

Contents lists available at ScienceDirect

Gondwana Research

journal homepage: www.elsevier.com/locate/gr

Fluid-rock interaction modeling to constrain Au enrichment: Implication for the giant Jiaodong Au mineralization, eastern North China Craton

Huan-Long Hu [a], Hong-Rui Fan [b,c,*], Ting-Guang Lan [a,c], Xue-Feng Yu [d], Da-Peng Li [d], Kui-Feng Yang [b,c]

[a] State Key Laboratory of Ore Deposit Geochemistry, Institute of Geochemistry, Chinese Academy of Sciences, Guiyang 550081, China
[b] Key Laboratory of Mineral Resources, Institute of Geology and Geophysics, Chinese Academy of Sciences, Beijing 100029, China
[c] College of Earth Science, University of Chinese Academy of Sciences, Beijing 100049, China
[d] Shandong Institute of Geological Sciences, Jinan 250013, China

ARTICLE INFO

Article history:
Received 9 November 2022
Revised 28 June 2023
Accepted 22 July 2023
Available online 24 August 2023
Handling Editor: Richard Palin

Keywords:
Fluid-rock interaction modeling
Wallrock alteration
Gold enrichment
Metasomatized lithospheric mantle
Jiaodong Peninsula

ABSTRACT

The devolatilization model of the metasomatized lithospheric mantle without pre-enriched gold has been proposed to account for the giant gold mineralization. An excellent example is the world-class Jiaodong gold province with >5000 tonnes Au resources in the eastern North China Craton. The auriferous fluid transport and gold enrichment during wallrock alterations are two vital processes to determine the giant gold mineralization formation in this province. However, the effects of the fluid-rock interaction with alterations on the auriferous fluid transport and gold enrichment still keep poor understanding, which leads the above model to be imperfect. The giant Jiaojia goldfield in this province recorded a wallrock alteration evolution from K-feldspar alteration to pyrite-sericite-quartz alteration, and some parts of the latter can become gold orebodies when the gold grade is >1 ppm. This study conducts thermodynamic fluid-rock interaction modeling to reveal auriferous fluid transport and coupled relationship between gold enrichment and alteration mineral assemblage based on the alteration-mineralization and ore fluid characteristics of the goldfield. The modeling of fluid-rock interaction with cooling indicates the transformation of Au-Cl complexes to Au-S complexes combined with the total sulfur concentration decrease by pyrite precipitation when cooling from ~460 °C can trigger the dispersive gold precipitation, which should hinder the gold long-range transport to lower ambient temperature. The high oxygen fugacity at >400 °C can enhance Au-Cl complexes stability, and the low pH can maintain high total sulfur concentration in the auriferous fluid, both of which facilitate the long-range gold transport to a lower-temperature environment. The auriferous fluid would acquire higher pH by the buffering of feldspars or sericite, which was beneficial for the high-efficiency precipitations of pyrite and gold. The ankerite-siderite assemblage without pyrophyllite in the pyrite-sericite-quartz alteration zone indicates that a cumulative fluid to rock mass ratio (f/r) of 3.8–4.8 should be needed for the transformation from K-feldspar alteration to pyrite-sericite-quartz alteration according to the fluid-rock interaction modeling at 300 °C and 2000 bar. In the case of auriferous fluids with ≤200 ppb Au concentration, the single fluid-rock interaction can only elevate the gold grade to ≤0.69–0.87 ppm in the pyrite-sericite-quartz alteration zone at f/r 3.8–4.8. Therefore, the fracture-induced fluid flow coupled with fluid-rock interaction is proposed to the prerequisite to elevate the gold grade to >1 ppm in the pyrite-sericite-quartz alteration zone. The metasomatized lithospheric mantle volume for the required ore fluid and Au in the Jiaodong province is estimated according to the modeling results and alteration-mineralization characteristics, which provides a link between the mantle without abnormal Au enrichment and the alteration-mineralization processes.

1. Introduction

Optimizing the exploration strategies and regional targeting for gold deposits is necessary due to its economic attribute and global demand. The re-fertilized sub-continental lithospheric mantle is proposed to play a significant role on the formation of giant gold

* Corresponding author at: Institute of Geology and Geophysics, Chinese Academy of Sciences, Beijing 100029, China.
E-mail addresses: fanhr@mail.iggcas.ac.cn (H.-R. Fan), lantingguang@126.com (T.-G. Lan).

https://doi.org/10.1016/j.gr.2023.07.015
1342-937X/

deposits (Hronsky et al., 2012; Griffin et al., 2013; Groves et al., 2019; Holwell et al., 2019; Deng et al., 2020; Wang et al., 2020), besides the supracrustal sources of sedimentary and igneous rocks (Goldfarb et al., 2001; Phillips and Powell, 2010; Tomkins, 2013; Patten et al., 2020). Global lithospheric mantle contains a main gold content range of 0.6–2.2 ppb with a median 1.2 ppb (Saunders et al., 2018). The localized anomalous gold contents (up to 13.8–41.2 ppb) and nanoparticles imply the refertilization of metasomatized lithospheric mantle should be a critical control on the giant gold mineralization (Hronsky et al., 2012; Holwell et al., 2019; Choi et al., 2020; Chen et al., 2022). However, whether an anomalous gold endowment in the metasomatized lithospheric mantle is essential for the giant Au mineralization still remains obscure. (Hronsky et al., 2012; Saunders et al., 2018; Choi et al., 2020; Wang et al., 2020). Recent studies reveal that the metasomatized lithospheric mantle and its derived magmas in the Jiaodong Peninsula of the eastern North China Craton (NCC) show no anomalous Au enrichment (a main range ~0.1–3 ppb; Wang et al., 2020, 2022a). They are still suggested to provide the main Au required for the Mesozoic giant gold mineralization in the NCC (Deng et al., 2020; Wang et al., 2020, 2022a). If this model is true, the exploration targets can be remarkably expanded to a larger area.

However, the above model is imperfect because the wallrock alteration effects on the auriferous fluid transport-gold enrichment processes still keep unclear. Firstly, the gold solubility is sensitive to the variations of oxygen fugacity, pH, total sulfur and Fe concentrations, and Au-bearing complexes during fluid-rock interaction with cooling or phase separation (Mikucki, 1998; Heinrich, 2005; Stefánsson and Seward, 2004; Evans et al., 2006; Pokrovski et al., 2014), which powerfully affect the gold transport and precipitation. The main gold deposits (e.g., Jiaojia and Sanshandao deposits) in the Jiaodong province are characterized by the intense fluid-rock interaction with wallrock alteration zonation, in which the disseminated- and stockwork-style gold ores belong to pyrite-sericite-quartz alteration rock (Li et al., 2013a, 2015; Hu et al., 2020a; Deng et al., 2020). Although previous studies have proposed the sulfidation with abundant pyrite precipitation is the important gold precipitation mechanism during pyrite-sericite-quartz alteration in this province (Xu et al., 2016; Yang et al., 2017; Deng et al., 2020), the fluid-rock interaction effects on gold transport and precipitation need be still clarified to better understand the gold enrichment processes. Secondly, the alteration mineral assemblage corresponds to a quantitative alteration progress with the necessary f/r at local fluid-rock equilibrium (Dolejš and Wagner, 2008; Mernagh and Bierlein, 2008; Reed et al., 2013; Xu et al., 2016; Li et al., 2022). This means the amount of cumulative Au in the mineralizing sites is limited by the ore fluid amount and alteration mineral assemblage, especially in the case the alteration zone itself becomes an orebody. Whether the limited auriferous fluid amount can enrich the giant gold mineralization remains unclear considering the metasomatized mantle without abnormal Au enrichment. Therefore, revealing the fluid-rock interaction effects on the auriferous fluid transport and coupled relationship between alteration and gold enrichment can help to understand the giant gold mineralization processes.

The disseminated- and stockwork-style mineralization contributes the major gold resources for the Jiaodong province (Deng et al., 2020; Fan et al., 2021). The Jiaojia goldfield is one of the most typical cases for the disseminated- and stockwork-style mineralization in this province due to its orebodies also belong to the alteration zone, which provides a perfect object to research the fluid-rock interaction processes in giant gold mineralization related with the metasomatized lithospheric mantle. The mineralization occurs at ~120 Ma (Zhang et al., 2020) without latter hydrothermal overprinting, which preserves the "fresh" and whole alteration-mineralization processes. Therefore, combining with the previous research data of alteration, mineralization and ore fluids in the Jiaojia goldfield (e.g. Song et al., 2010, 2014; Wei et al., 2015, 2019; Yang et al., 2017; Hu et al., 2020a, b), this study conducts the detailed alteration mineral identification and thermodynamic modeling of fluid-rock interaction to reveal the fluid-rock interaction effects on the auriferous fluid transport and the coupled relationship of wallrock alteration-gold enrichment. The results further provide a quantitative link between the metasomatized lithospheric mantle without abnormal Au enrichment and shallow alteration-mineralization processes.

2. Regional geology

The NCC is one of the oldest cratons around the world, which experienced multiple subduction and collision events during the Neoarchean and Paleoproterozoic (Zhai and Santosh, 2011). The south margin of the NCC was subducted and metasomatized by the Yangtze Craton during Late Triassic (Zheng et al., 2003). The eastern part of the NCC experienced the Paleo-Pacific plate subduction and rollback since the Early Jurassic (Jiang et al., 2010; Wu et al., 2019; and references therein), leading to mantle metasomatism and decratonization with asthenosphere upwelling, structure activities and extensive magmatism (Cai et al., 2013; Deng et al., 2017; Wu et al., 2019; Yang and Santosh, 2019).

The Jiaodong Peninsula is located along the southeastern margin of the NCC. It is divided into the Jiaobei terrane in the west and the Sulu ultrahigh-pressure metamorphic belt in the east (Fig. 1). The Jiaobei terrane is divided into the Jiaobei uplift in the north and the Jiaolai basin in the south. The Late Jurassic biotite granite (~160 Ma, Yang et al., 2012) and the Early Cretaceous granitoids (130–108 Ma, Li et al., 2019 and references therein) were emplaced in the Jiaobei terrain. Mafic-intermediate igneous rocks occur throughout the Jiaobei terrain (e.g. 128–117 Ma lamprophyre and diorite dikes; Cai et al., 2013; Deng et al., 2017). Most of these mafic-intermediate igneous rocks are corroborated to be derived from the metasomatized lithospheric mantle (Cai et al., 2013; Yang et al., 2014; Deng et al., 2020).

The enormous gold mineralization occurred at ~120 Ma in the Jiaodong Peninsula (Zhu et al., 2015; Cai et al., 2018; Zhang et al., 2020). The regional NE-NNE-striking Sanshandao-Cangshang, Jiaojia-Xincheng and Zhaoyuan-Pingdu fault zones are distributed in the Jiaobei uplift, and control almost all gold deposits in the northwest Peninsula (Fig. 1). Two types of gold deposits including the disseminated and stockwork type (e.g. Jiaojia, Xincheng, Sanshandao and Dayingezhuang) and the sulfide-bearing quartz vein type (e.g. Linglong) occur in these three fault zones (Fan et al., 2021).

3. Deposit Geology

3.1. Local geologic setting

The Jiaojia goldfield consists of the Jiaojia, Sizhuang and Wang'ershan gold deposits, and the deep exploration areas of Matang, Qianchen, Shaling, Zhaoxian and Wuyi village (Fig. 2a–c; Fig. 3a–d; Song et al., 2017; Zhu et al., 2018; Yu et al., 2019). The goldfield has the total gold reserves of ~1400 tonnes and newly predicted gold resources of 900 tonnes (Song et al., 2014, 2017; Zhu et al., 2018; Yu et al., 2019). It is controlled by the NE-striking and NW-dipping Jiaojia fault zone (Fig. 2a–b). The hanging wall of the fault zone comprises Archean metamorphic rocks and the footwall consists of Late Jurassic Linglong biotite granite (Fig. 4a–f; Hu et al., 2020a).

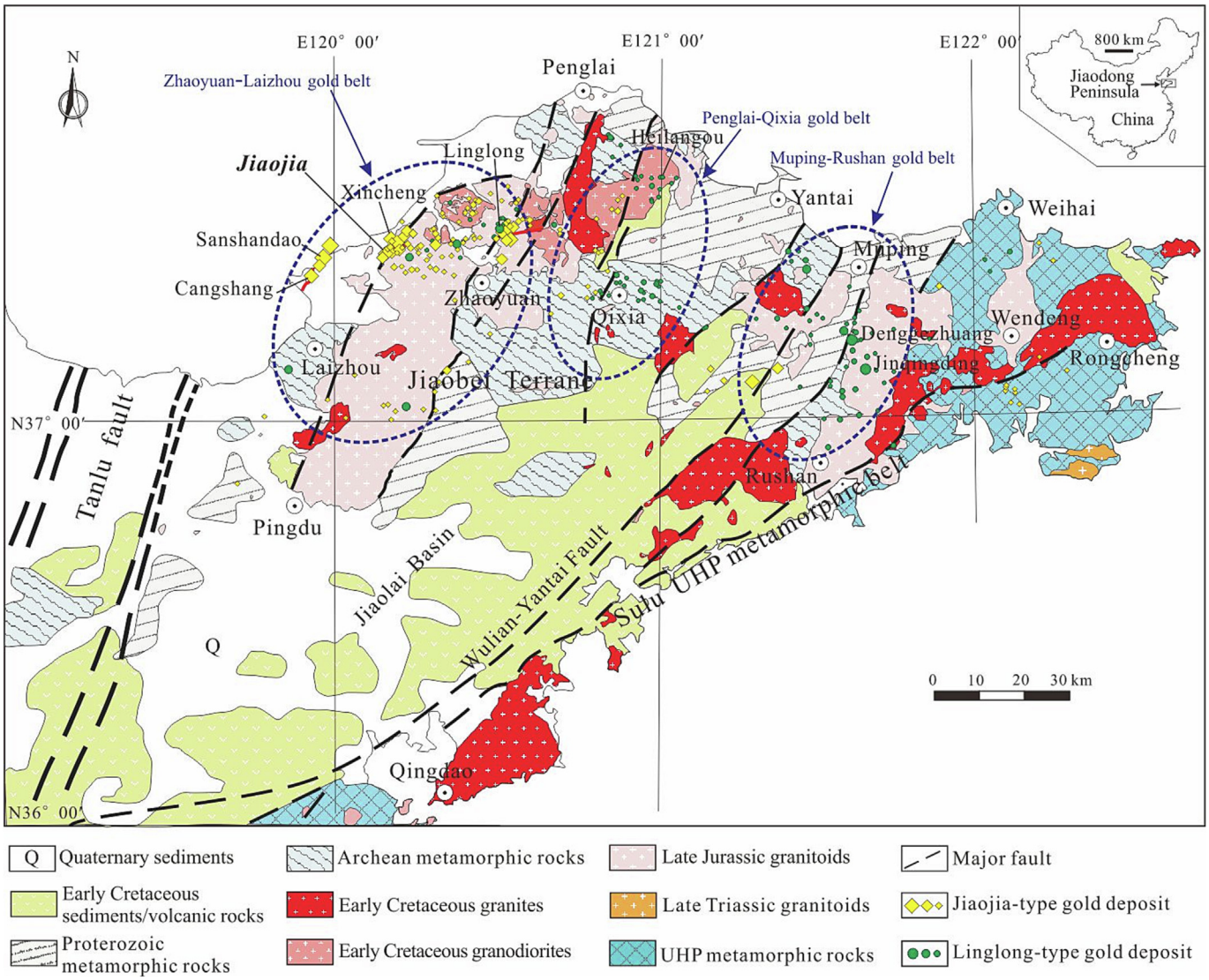

Fig. 1. Geological map of the Jiaodong Peninsula (Modified after Fan et al. (2021)).

3.2. Orebody characteristics

Orebodies of the Jiaojia goldfield are mainly hosted by the altered Linglong granite in the footwall (Fig. 2b–c). They occur in a vertical depth range of 0 to −2855 m, extending up to ~6756 m along dipping direction (Fig. 3a–b; Supplementary Data 1 Table S1; Song et al., 2014; Yu et al., 2019). The vast majority of gold mineralization is hosted by pyrite-sericite-quartz alteration zone (Song et al., 2014; Yu et al., 2019). The main orebodies pinch out, intersect or interconnect in the horizontal and vertical projection maps of the Jiaojia goldfield (Fig. 3a–b; Song et al., 2014). The fineness of Au grains (wAu/(wAu + wAg) × 1000) mainly ranges in 771–909 (Table S1).

The Jiaojia gold deposit consists of the No. I and III orebodies (Fig. 2b–c). The No. I orebody is parallel to the main fault and contributes ~87% gold resources (~205 tonnes; Fig. 2b; Song et al., 2010, 2011). It is characterized by disseminated- to stockwork-style mineralization in pyrite-sericite-quartz alteration zone (Fig. 4d–f). The orebody has the strike and inclined lengths of about 960 m and 1370 m, respectively (Table S1). And the average true thickness of it is ~10.95 m (Table S1). The gold grade concentrates in 1–4 ppm with an average 3.74 g/t (Fig. 3c; Song et al., 2010). The No. III orebody is characterized by vein- and stockwork-style mineralization that crosscuts K-feldspar alteration zone (Fig. 2b–c; Hu et al., 2020a).

3.3. Hydrothermal alterations and mineral paragenesis

K-feldspar alteration, sericitization, silicification and pyrite-sericite-quartz alteration zones occur progressively from the fresh Linglong granite to the main fault face in the Jiaojia goldfield (Fig. 2b–c; Fig. 4a–f). This alteration zonation pattern extends stably to the depth of about −2855 m below the ground (Table S1). K-feldspar, albite, sericite, quartz, calcite, siderite, ankerite, pyrite, gold, chalcopyrite, galena, sphalerite and pyrrhotite are the common minerals in these alteration zones (Fig. 5a–i; Table S1).

Extensive pink K-feldspar alteration overprinted on the fresh Linglong granite, in which the hydrothermal K-feldspar and quartz account for >60% of the total rock volume (Fig. 2b; Fig. 4a; Fig. 5a–b). The isolated and euhedral pyrite grain can be observed in this alteration zone, which coexists with quartz, calcite, sericite, zircon and rutile in the local area (Fig. 5d). Grey sericitization zone surprinted on K-feldspar alteration zone and consists of quartz (>60% of the total rock volume), sericite (<40% of the total rock

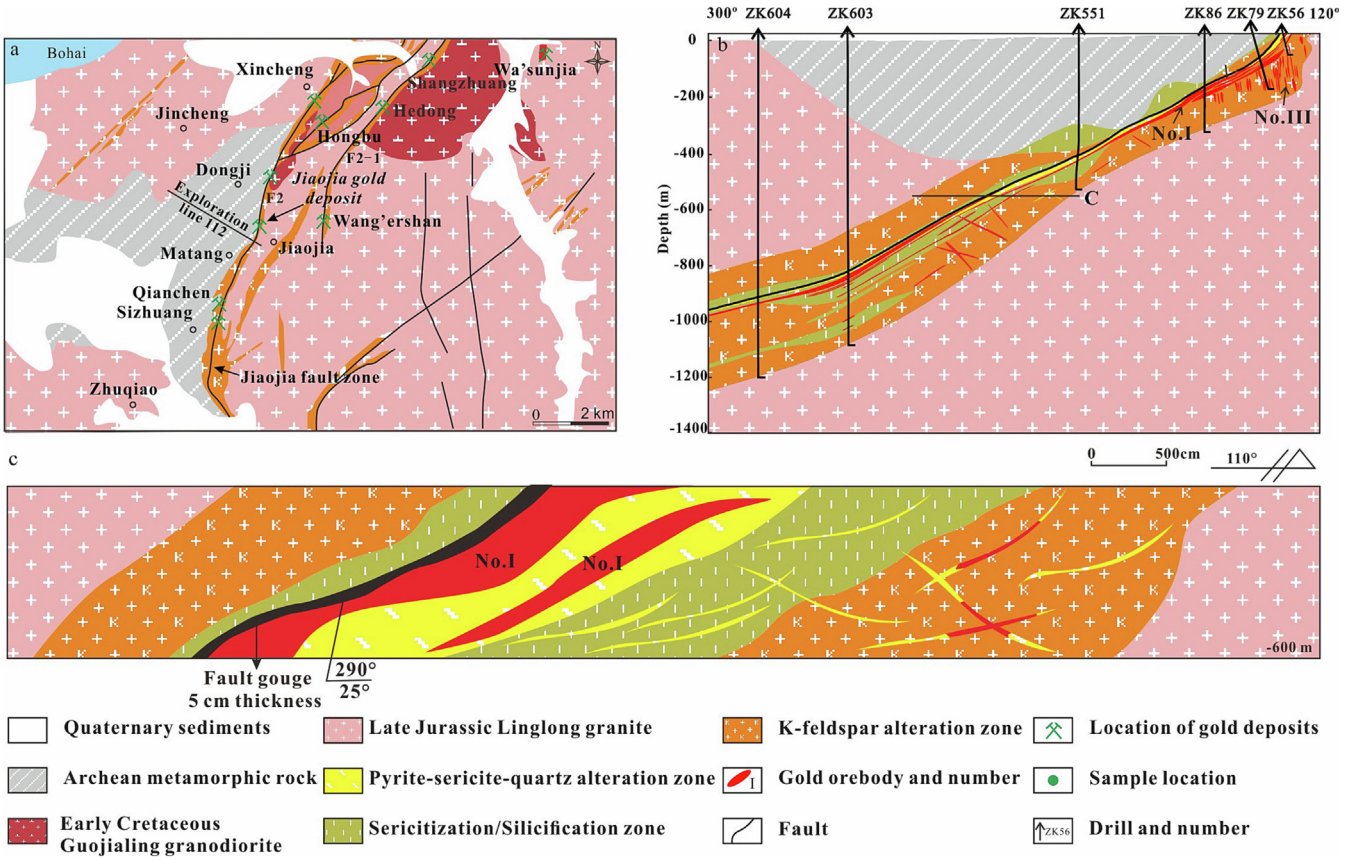

Fig. 2. (a) Geologic map of the Jiaojia-Xincheng gold camp (Modified after Song et al. (2011)). (b) The vertical geologic cross section of the No. 112 exploration line (Modified after Song et al. (2010)). (c) The geologic cross-section at the depth of ~ 600 m (correspond to the line in the Fig. 2b), illustrating the hydrothermal alteration zonation and mineralization.

volume) and minor carbonates (Fig. 2b–c; Fig. 4b; Fig. 5e). White quartz vein with a little pyrite belongs to silicification and crosscuts K-feldspar alteration zone (Fig. 4c).

The dark grey pyrite-sericite-quartz alteration zone shares the similar structural, compositional and geochemical characteristics with the sericitization zone, except the former contains higher contents of pyrite, gold and polymetallic sulfides according to this study and Zhang et al. (2014). This alteration overprinted on K-feldspar alteration zone (Fig. 2b–c; Fig. 4a, d). Pyrite-sericite-quartz stockworks crosscut K-feldspar alteration zone with albite replacement around K-feldspar rim in the weak fluid-rock interaction sites (Fig. 4a, d). The albite is easier to be altered as sericite than K-feldspar as alteration enhancement (Fig. 5a–c). The ankerite and calcite can also coexist with K-feldspar, albite, sericite and quartz (Fig. 5b–c). Pyrite-sericite-quartz alteration also surprinted on sericitization and silicification zones (Fig. 2c; Fig. 4b, e). Feldspars were replaced by sericite and quartz and micro-textures of previous minerals were not preserved (Fig. 5f). Euhedral to subhedral pyrite occurs as disseminated and stockwork styles and takes up ~5% of the rock volume (Fig. 4d–f; Fig. 5f–i). The quartz-pyrite stockworks contain pyrite by 60–95% of the total stockwork volume (Fig. 4e; Fig. 5h–i). Gold grains are wrapped by pyrite grains or crosscut pyrite veins (Fig. 5h–i). Chalcopyrite and sphalerite crosscut pyrite veins, and ankerite grains are wrapped by sphalerite (Fig. 5h–i; Fig. 6). Then pyrite veins and sphalerite veins are crosscut by siderite veins. Galena veins crosscut pyrite veins, sphalerite veins and siderite veins (Fig. 6a). Pyrite, ankerite and siderite can also coexist as the stockworks in the pyrite-sericite-quartz alteration zone (Fig. 4f; Supplementary Data 2 Fig. S1). The polymetallic sulfides are only minor relative to pyrite in the pyrite-sericite-quartz alteration zone and pyrite stockworks, considering the visible pyrite grains and veins in the hand specimens (Fig. 4a–f) and local thin polymetallic sulfide veinlets crosscutting pyrite grains and veins under the microscope (Fig. 5h–i; Fig. 6a). Finally, quartz-calcite veins crosscut pyrite-sericite-quartz alteration zone and metal mineral veins (Fig. 5f; Fig. 6a). Five alteration stages with the mineral paragenesis are summarized in Fig. 7.

4. Methods

4.1. Analytical methods for minerals

Rock samples in K-feldspar alteration, sericitization, silicification and pyrite-sericite-quartz alteration zones were collected from the Jiaojia goldfield and polished for petrographic studies. Back scattered electron (BSE) images were obtained with Nova Nano scanning electron microscope (SEM) 450 at the Institute of Geology and Geophysics, Chinese Academy of Sciences (IGGCAS), and the SKLODG, Institute of Geochemistry, Chinese Academy of Sciences (IGCAS). An accelerating voltage of 15 kV and a primary beam current of 20nA are set during SEM imaging. The instrument is equipped with an X-MAXN80 Energy-Dispersive X ray Spectrometer (EDS) detector, which is used for semi-quantitative spot analyses and elemental mapping. Raman analyses with LabRam HR Laser confocal Raman spectroscopy was also used for mineral identification at IGGCAS and IGCAS.

Major elements of K-feldspar and albite were analyzed using a JOEL JXA 8230 Electron Probe Microanalysis (EPMA) at the SKLODG, IGCAS. An accelerating voltage of 25 kV and a beam cur-

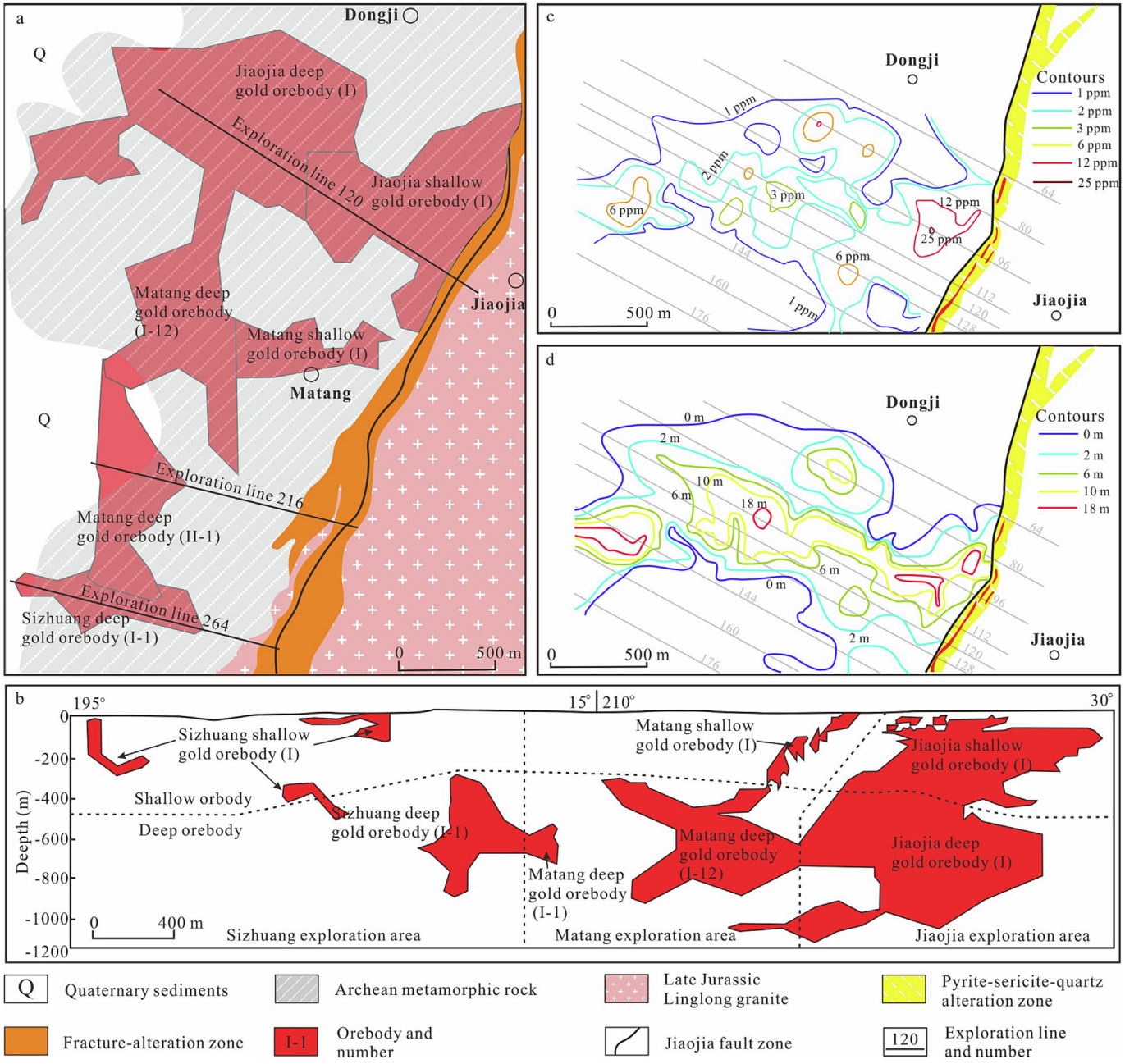

Fig. 3. The distribution of main orebodies in the Jiaojia goldfield. (a) The horizontal projection of main orebodies (Song et al., 2011). (b) The vertical projection of main orebodies along the Jiaojia fault zone (Song et al., 2011). (c) The contours of Au grade of the No. I orebody (Song et al., 2010). (d) The contours of thickness of the No. I orebody (Song et al., 2010).

rent of 10nA are set during the analysis. The matrix correction was carried out by the ZAF program. Mineral standards of orthoclase (Na and K), diopside (Ca), almandine (Fe, Mn, Al, Mg and Si) and pyrope (Ti and Cr) were used for analytical result calibration. The detection limits for the major elements are better than 0.01 wt%. All the electron microprobe analysis results for feldspars are presented in Supplementary Data 1 Table S2.

4.2. Whole-rock geochemistry and bulk fluid composition determination

Major and partial trace (Cr, Cu, Ba, Ni, Sr, V, Zr, Zn) elements contents of one Linglong granite, four K-feldsparation rocks, four sericitization rocks and seven pyrite-sericite-quartz alteration rocks were determined at the IGGCAS and shown in Supplementary Data 1 Table S3. The 0.5 g whole-rock powder of every sample mixed with 5 g $Li_2B_2O_7$ + $LiBO_2$. These mixtures were heated and melted into glass disks and analyzed by X-ray fluorescence spectroscopy (XRF) with an AXIOS-Minerals spectrometer. The analytical uncertainties were generally within 0.1–1% (RSD). Loss on ingition (LOI) was obtained using 0.5 g powder heated up to 1100 °C for one hour.

Seven white quartz vein samples of silicification stage from the Jiaojia goldfield were collected for bulk fluid composition determination by decrepitation of hosted fluid inclusions at the IGGCAS. Concentrations of major ions Cl^-, K^+, Na^+, and Ca^{2+} were analyzed by HIC-6A C-R5A ion chromatography. The detection limits for the concentrations of these ions are ~0.05 ppm. Concentrations

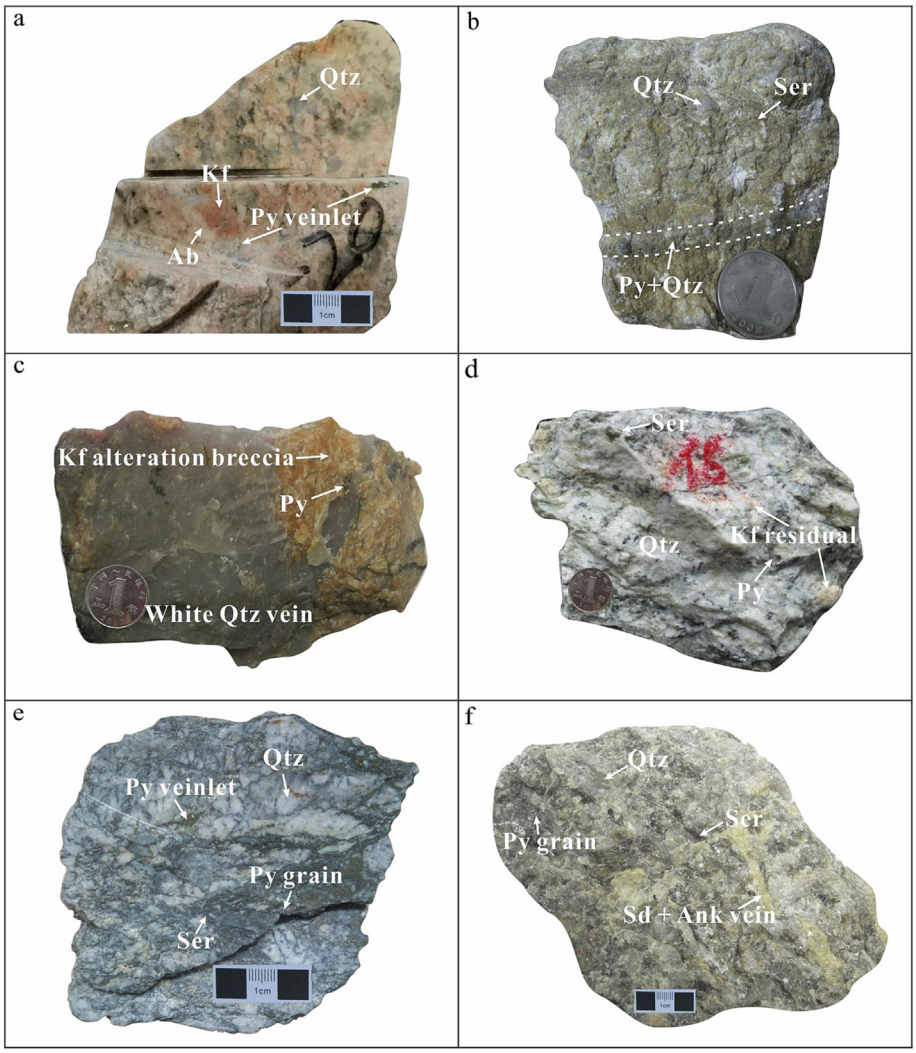

Fig. 4. The photographs of hand specimens show the characteristics of hydrothermal alteration and mineralization. (a) K-feldspar alteration rock with albite around K-feldspar grains and pyrite veinlets. (b) Sericitization rock with quartz gravels and latter quartz-pyrite vein crosscut. (c) The white quartz veins with a little pyrite crosscut K-feldspar alteration zone. (d) Pyrite-sericite-quartz alteration zone with the K-feldspar alteration rock residual. (e) Silicification with cataclastic white quartz gravel, and crosscut by pyrite-sericite-quartz stockworks. (f) Pyrite-sericite-quartz alteration zone with pyrite and carbonates veinlets. Abbreviations: Ab = albite, Ank = ankerite, Kf = K-feldspar, Py = pyrite, Qtz = quartz, Sd = siderite, Ser = sericite. These abbreviations are also used in the next illustrations.

of major vapor phases H_2O, CO_2 and H_2S were analyzed by RG202 quadrupole mass spectrometer. The gas collection was carried out by heating samples at vacuum (10^{-6} Pa). The reproducible concentrations for CO_2 and H_2S in the previous bulk fluid composition analysis of quartz samples can be low to 0.5 mol.% and 0.0035 mol.%, respectively. The method details are shown in Li et al. (2013b). The analytical results are shown in Supplementary Data 1 Table S4.

4.3. Thermodynamic modeling

(1) The flow-through leaching and cooling modeling The consistent H-O isotopic compositions of quartz from silicification and pyrite-sericite-quartz alteration stages indicate the ore fluids for these two stages shared a common source in the Jiaojia goldfield (Guo et al., 2014; Wei et al., 2015; Yang et al., 2017). The H-O isotopic exchange calculation between the ore fluid and Linglong granite suggests an average f/r 0.1 is reasonable during the pyrite-sericite-quartz alteration stage in this goldfield (Guo et al., 2014). The auriferous fluid flew through micro-fractures in the K-feldspar alteration zone of different depths to eventually form the gold-fertile pyrite-sericite-quartz alteration zone (Fig. 4a, c and d; Fig. 5a–f), or locally focused into dilated sites to precipitate auriferous quartz-sulfide veins in this goldfield (Yang et al., 2017; Hu et al., 2020a). The precipitation of pyrite and gold from the auriferous fluid could occur at ≥300 °C considering the pressure correction for trap temperature of fluid inclusions in the ore-related quartz veins (Fan et al., 2003; Yang et al., 2017). A pressure of 2000 bar should be closer to the hydrostatic to lithostatic pressure during pyrite-sericite-quartz alteration stage considering the ~500–2000 bar trap pressure for the fluid inclusion in ore-related quartz of the Jiaojia goldfield (Wei et al., 2015; Yang et al., 2017). Therefore, the one-dimensional flow-through leaching modeling and cooling modeling (e.g., Heinrich et al., 1996; Mernagh and Bierlein, 2008; Petrella et al., 2021; Li et al., 2022) are adopted to calculate the coupled relationship between alteration mineral assemblage variation and gold transport-enrichment during the transformation from K-feldspar alteration to pyrite-sericite-quartz alteration with fluid-rock interaction and cooling (Fig. 8).

The flow-through model assumes the local equilibrium between successive small batches of fluid and a reactive rock cell

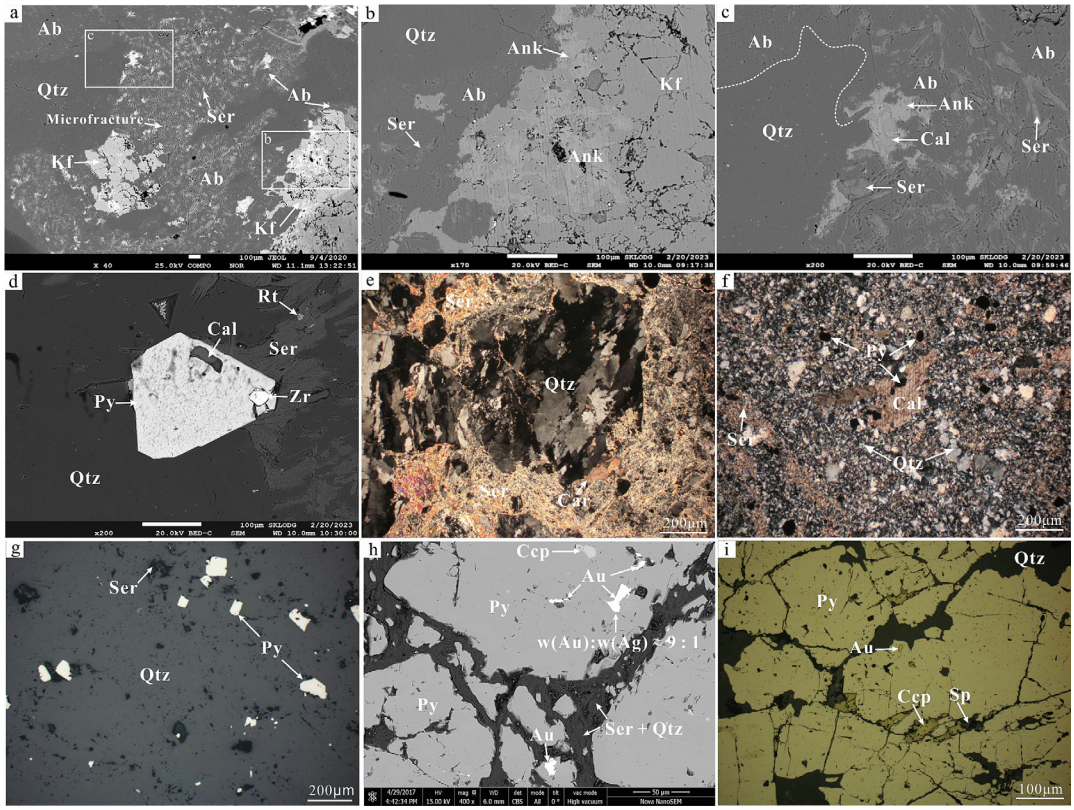

Fig. 5. BSE images (a–c and h) and optical micrographs (d–g and i) for mineral assemblages in the hydrothermal alteration zones. (a)–(c) The K-feldspar alteration zone with later pyrite-sericite-quartz alteration overprint and albite crystallization, the stronger sericite-quartz alteration of albite than K-feldspar with the fluid-rock interaction enhancement, the crystallization of ankerite and calcite during sericite-quartz alteration, and the Fig. 5b and 5c corresponding to the fig. b and c in Fig. 5a. (d) The isolated and euhedral pyrite grain in K-feldspar alteration zone, coexisting with quartz, calcite, sericite, zircon and rutile. (e) The complete replacement of feldspars by sericite and quartz with a few carbonates in sericitization zone. (f) and (g) Minerals were completely broken and altered in pyrite-sericite-quartz alteration zone, with some late calcite veinlets crosscut. (h) and (i). Gold grains in pyrite veinlets, with quartz, sericite, chalcopyrite and sphalerite crosscut, w(Au):w(Ag) refers to the mass ratio of Au and Ag. Abbreviations: Cal = calcite, Car = carbonates, Ccp = chalcopyrite, Rt = rutile, Sp = sphalerite, Zr = zircon.

(Fig. 8a). The sulfidation processes are simplified as the pyrite precipitation during the modeling considering the pyrite precipitation is one of the main gold precipitation mechanisms in the Jiaojia goldfield (Yang et al., 2017; Fan et al., 2021). In the model, the initial auriferous fluid flows through the initial K-feldspar alteration rock cell and experiences fluid-rock interaction with sulfidation at f/r 0.1, 300 °C and 2000 bar. After the first simulation run, the residual barren ore fluid is expelled and the initial auriferous fluid flows through the altered K-feldspar alteration rock cell again (Fig. 8a). This simulation process is repeatedly for f/r from 0.1 to 6.0. These modeling results represent the final phase equilibrium states of fluid-rock interaction with different f/r values when the chemical system cools to 300 °C and 2000 bar. The reaction processes of the 27th and 40th fluid-rock modeling are taken for the cooling modeling with the ambient alteration mineral assemblage at 500–250 °C and 2000 bar considering the ore fluid temperature could be up to ~500 °C in the Jiaodong gold deposits (Fig. 8b–c; Fan et al., 2003). On the one hand, these two modeling projects can give the alteration mineral assemblage evolution and gold transport-precipitation processes during cooling with different reaction wall-rocks. On the other hand, the choices of these two reaction processes can help to reveal the cooling effect on the disappearance temperatures of feldspars and carbonates. The equilibrium of minerals and aqueous species for the initial auriferous fluid is also simulated at 500–250 °C and 2000 bar, which fits the ore vein environment (Fig. 8d).

(2) The constraints for the compositions of the initial rock and auriferous fluid The initial K-feldspar alteration rock cell composition for the first calculation run is referenced from the mass percentage contents of the four K-feldspar alteration samples (Table S3). The Ti, Mn, Mg and phosphorus are omitted due to their extremely low contents in the analyzed K-feldspar alteration rock samples. The sulfur content cannot be measured for the alteration rocks samples considering the sulfur loss during the analytical glass disk preparation with heating and melting. The Fe content of the total Fe_2O_3 contents is approximatively used to calculate the pyrite content for the initial K-feldspar alteration rock cell. A little pyrite addition into K-feldspar alteration rock cell could be acceptable and should not give the large effect on the chemical system, because the pyrite phase can be stable in the local area of this alteration rock during the initial stage of fluid-rock interaction between the ore fluid and K-feldspar alteration rock (Fig. 5d). The gold content is set to 0 considering the low Au content range of 0.4–98 ppb in the Linglong granite and K-feldspar alteration rocks relative to that in the pyrite-sericite-quartz alteration zone (1.71–6.25 ppm) of the Jiaojia goldfield (Supplementary Data 1 Table S5; Song et al., 2011; Zhang et al., 2014). The Cu (0.32–724.3 ppm), Pb (14.5–2188.0 ppm), Zn (8.4–1499.0 ppm) and As (0.1–94.3 ppm) contents are far less than the Fe content (0.33–6.76 wt%) in the fresh Linglong granite and alteration zones (Table S5; Zhang et al., 2014). Therefore, the Cu, Pb, Zn and As contents are set to 0 for the initial K-feldspar alteration rock cell. In the end, the whole rock composition was normalized to 100 g in the SiO_2-Al_2O_3 -CaO-Na_2O-K_2O-Fe-S composition space (Table 1).

Four Au concentrations of 20 ppb, 50 ppb, 100 ppb and 200 ppb are set for the initial auriferous fluid to calculate the gold enrichment

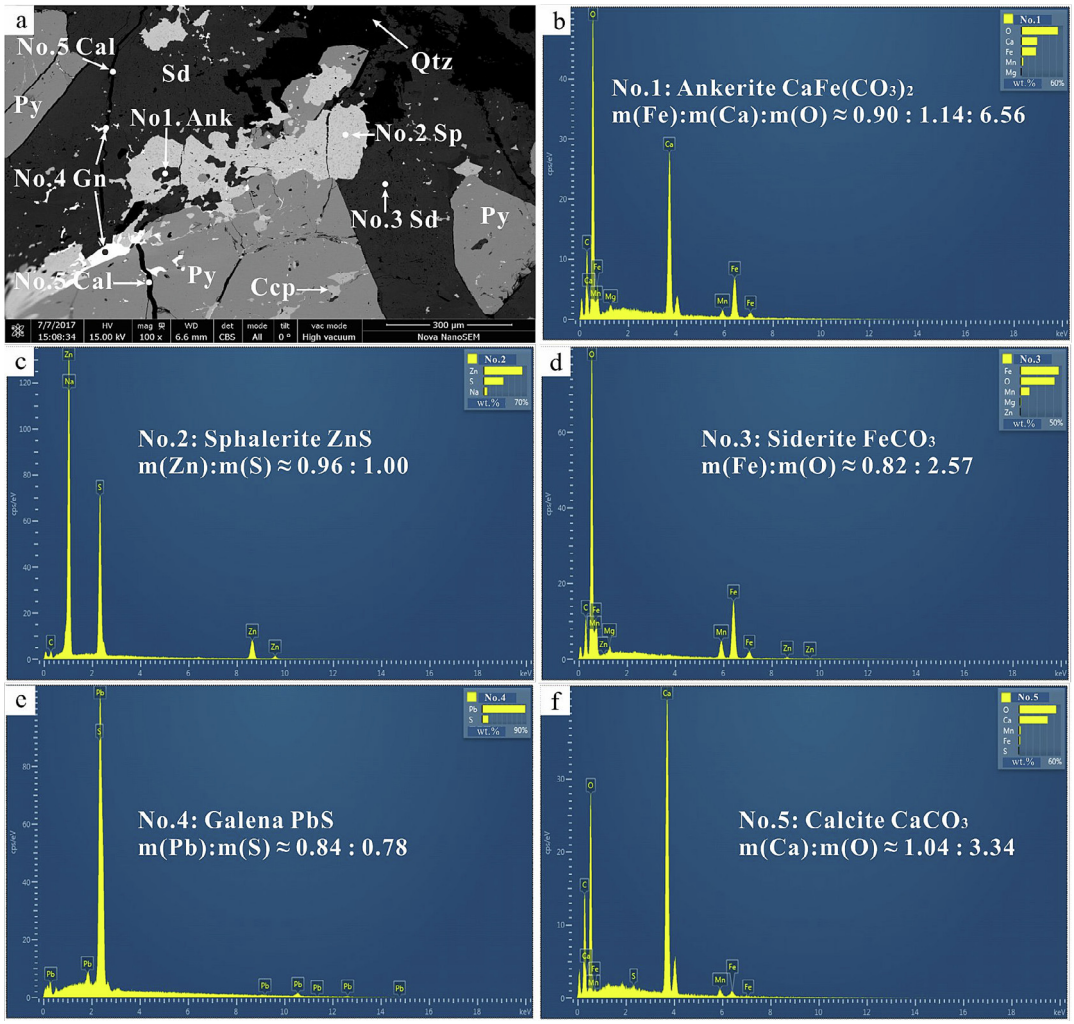

Fig. 6. The mineral identification results by BSE-EDS, in which the ratios represent the atomic mole ratios. The BSE image is taken from Hu et al. (2020a). Gn = galena.

amount during flow-through modeling (Table 1), according to the magmatic and metamorphic fluids usually contain ~20–200 ppb gold (Ulrich et al., 1999; Rauchenstein-Martinek et al., 2014; Petrella et al., 2020; McLeish et al., 2021). The H_2S concentrations are lower than 0.01 mol/kg H_2O by crush-leach analysis of quartz-hosted fluid inclusions in the silicification stage of the Jiaojia goldfield (Table S4). The analyzed H_2S concentrations might be lower than the real values due to the secondary fluid inclusions dilution and pyrite precipitation. The H_2O-CO_2-NaCl fluids can absorb sulfur from sources during metamorphic devolalitization and magmatic hydrothermal processes, which leads to a large sulfur concentration range of 0.006–0.2 mol/kg H_2O (Kouzmanov and Pokrovski, 2012; Rauchenstein-Martinek et al., 2014; Goldfarb and Groves, 2015). Here, an intermediate sulfur concentration of 0.08 mol/kg H_2O is set for the initial auriferous fluid (equal to 0.05 mol/kg initial auriferous fluid). The ore fluid at the Jiaojia goldfield is reduced with pyrrhotite precipitation, which indicates the dissolved H_2S is the main sulfur-bearing aqueous species in the ore fluid (Hu et al., 2020b). Therefore, the H_2S concentration in the initial auriferous fluid is set as 0.08 mol/kg H_2O. The bulk analysis of hosted fluid inclusions in the white quartz vein of silicification stage in the Jiaojia goldfield shows an average CO_2 concentration range of 13.0 mol.% (Table S4). The microthermometry study for the ore-related quartz-hosted fluid inclusions shows a CO_2 concentration range of 8.0–12.0 mol. % at the Jiaojia goldfield (Wei et al., 2015; Yang et al., 2017). Therefore, a reasonable 10 mol.% CO_2 concentration is set for the initial auriferous fluid. The salinity of the ore fluid concentrates at ~8 wt % NaCl eq. according to the fluid inclusion microthermometry and the fluid inclusion bulk composition analysis for the ore-related quartz veins at the Jiajia goldfield and the isogenetic Sanshandao gold deposit, in which the NaCl mole concentration is about 4 times as much as the KCl concentration (Table S4; Wei et al., 2015; Wen et al., 2016; Xu et al., 2016; Yang et al., 2017; Hu et al., 2021). The concentrations of NaCl and KCl are set to 1.4 mol/kg H_2O and 0.32 mol/kg H_2O, respectively. The concentrations of $CaCl_2$ and $FeCl_2$ are set to 0.01 mol/kg H_2O and 0.23 mol/kg H_2O, respectively, according to the bulk and individual analyses of fluid inclusion compositions in the ore-related quartz veins from this study and the isogenetic Sanshandao and Linglong gold deposits (Xu et al., 2016; Wang et al., 2022b). The concentrations of dissolved Si and Al are calculated to 0.04 mol/kg H_2O and 2×10^{-5} mol/kg H_2O by the exchange equilibrium between the initial auriferous fluid and K-feldspar alteration rock at 500 °C and 2000 bar, respectively.

(3) Thermodynamic modeling method The modeling for the flow-through and cooling processes was carried out using the GEMS code package (Wagner et al., 2012; Kulik et al., 2013). A thermodynamic dataset including H_2O, essential aqueous species and mineral end-members is presented in Supplementary Data 3. The chemical system definition Na–K–Ca–Fe–Al–Si–H–O–C–S–Cl–Au at interested pressure and temperature comes from the realistic

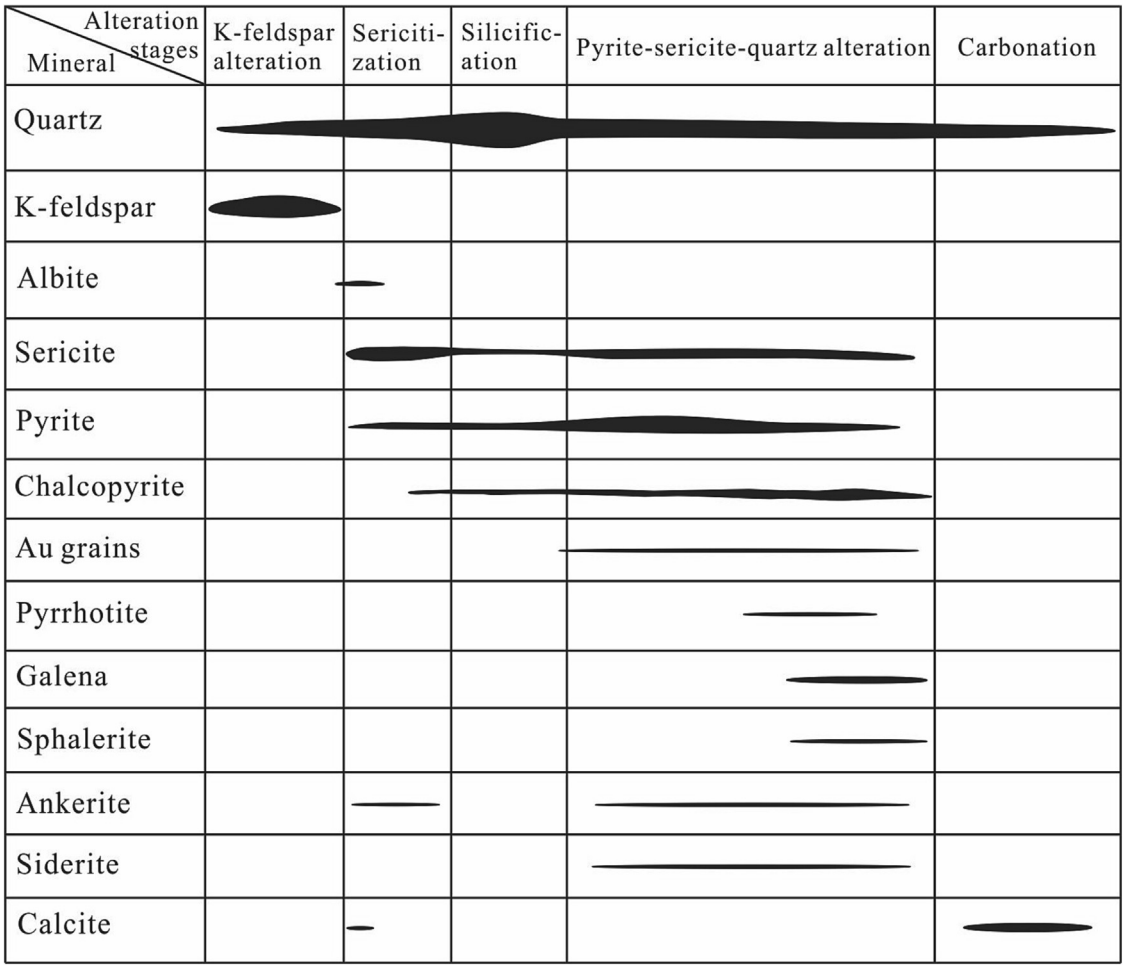

Fig. 7. Mineral paragenesis sequence of the Jiaojia gold deposit.

alteration-mineralization characteristics of the Jiaojia goldfield. The Na–K–Al–Si–H–O–Cl aqueous subsystem is adopted as skinny system (Miron et al., 2016), the aqueous species of which have been embed into the MINES thermodynamic database (Gysi, 2017). The sulfur aqueous species of molecular sulfurs, thiosulfate and polysulfide (e.g. S_3^-, S_8, $S_2O_3^{2-}$ and S_nS^{2-}) and their Au-bearing complexes (e.g. $AuHS(H_2S)^0$, AuS_3^0 and $Au(HS)S_3^-$) are not input in the thermodynamic dataset due to their minor effects or instability in the interested physicochemical conditions (See details in Discussion; Mei et al., 2013; Pokrovski and Dubessy, 2015; Pokrovski et al., 2015). A solid solution model of Van Laar asymmetric formalism with algorithm for plagioclase is adopted from Holland and Powell (2003) and Gysi (2017). Thermodynamic properties of aqueous species were calculated using the revised Helgeson-Kirkham-Flowers (HKF) equations of state (Tanger and Helgeson, 1988; Shock and Helgeson, 1988; Shock et al., 1989). Activity coefficients of aqueous species were calculated using the extended Debye–Hückel equation (Helgeson et al., 1981; Oelkers and Helgeson, 1990).

5. Results

5.1. Mineral identification and whole-rock analytical results

The native gold, pyrite, chalcopyrite, sphalerite, galena, sericite, ankerite, siderite, calcite, rutile and zircon are identified by BSE-EDS and Raman analyses (Fig. 5a–c, h; Fig. 6; Fig. S1). The EDS elemental mapping is carried out for schistose mineral assemblage in the pyrite-sericite-quartz alteration samples. The mapping shows the homogeneous Si Kαl, K Kαl and Al Kαl EDS information with the negligible Mg Kαl (Supplementary Data 2 Fig. S2). Other EDS information assemblage like the homogeneous Si Kαl and Al Kαl without K K αl has not been observed. The EDS mapping results indicate the schistose mineral is sericite. The pink K-feldspar has approximately pure $KAlSi_3O_8$, and the white mineral around the pink K-feldspar grains has approximately pure $NaAlSi_3O_8$, i.e. albite (Fig. 4a; Supplementary Data 2 Fig. S3). In addition, the modal volume compositions (vol.%) of the main mineral endmembers in these rocks are calculated and shown in Supplementary Data 2 Fig. S4 according to the results in Table S3.

5.2. Thermodynamic modeling results

5.2.1. Flow-through leaching modeling

The results are shown in Fig. 9a–h. Minor anhydrite exists in the altered K-feldspar alteration rock cell at cumulative f/r < 0.4 (hereafter the f/r indicates the cumulative f/r if not specified), and calcite disappears at f/r > 1.4 (Fig. 9a). Albite and K-feldspar disappear at f/r of 2.8 and 3.8, respectively. Quartz and sericite keep precipitation at f/r < 3.8, after which they start dissolving. Ankerite precipitates at f/r < 1.4 and is exhausted at f/r of 4.8. Siderite starts precipitating at f/r of 1.4 and starts dissolving at f/r of 4.8. Pyrophyllite begins to precipitate at f/r > 4.8 (Fig. 9a, d). Pyrite always precipitates throughout the leaching modeling (Fig. 9a, d). The Au

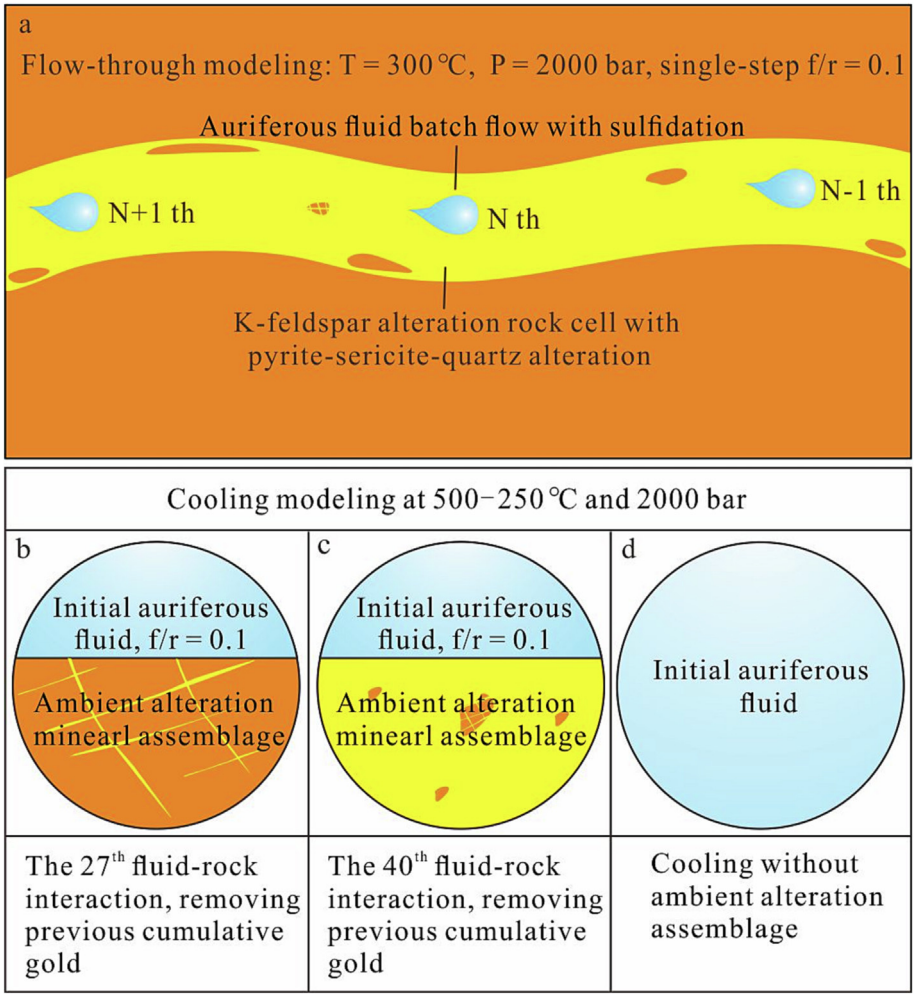

Fig. 8. The flow chart of fluid-rock interaction modeling.

Table 1
The initial auriferous fluid and rock compositions for the modeling.

Auriferous fluid components[a]	Concentration (mol/kg H_2O)	K-feldspar alteration rock cell	Content (wt.%)
CO_2	7 (10 mol.%)	SiO_2	76.37
NaCl	1.4 (5.6 wt%)	Al_2O_3	13.00
KCl	0.32 (1.5 wt%)	CaO	1.14
H_2S	0.08	Na_2O	3.47
SiO_2	0.05	K_2O	5.26
$FeCl_2$	0.23	FeS_2	0.76
$CaCl_2$	0.01		
$AlCl_3$	3.64E-05		
AuCl	2.00E-7/4.00E-7/8.00E-7/1.5E-6		

[a] Components expressed as neutral complexes without implying knowledge of actual speciation.

grades can be calculated out for the reacted rock cells at the specific f/r using the function expressions in Fig. 9b.

The auriferous fluid has a low $logfo_2$ of −36.3 at f/r > 0.4 (dissolved oxygen concentration in fluid, mol/kg H_2O), in which the H_2S^0 and HS^- are the dominated S-bearing aqueous species (Fig. 9c, g). It shows five pH steps of 4.72, 4.75, 4.36, 3.96 and 2.63 in f/r of 0.1–6.0, the leaps of which correspond to the disappearances of anhydrite, albite, K-feldspar and ankerite (Fig. 9a, c). The dissolution of these minerals also controls the step-shaped concentration variations of aqueous species (Fig. 9e–h). The $Au(HS)_2^-$ is the main Au-bearing complex at f/r of 0.4–3.8, and the $AuHS^0$ becomes the predominant Au-bearing complex at f/r of 3.8–6.0 (Fig. 9h).

5.2.2. Cooling modeling

(1) Cooling modeling for the 27th fluid-rock reaction process Alkali feldspar solid solution $(K,Na)AlSi_3O_8$ and anorthite (An, $CaAl_2Si_2O_8$) react to form plagioclase and pure K-feldspar (Kf) at ~453 °C (Fig. 10a). Plagioclase transforms to albite (Ab) due to An and Kf losses (Fig. 10a). Ankerite and siderite begin to precipitate at 447 °C and 425 °C, respectively (Fig. 10a). Pyrrhotite and magnetite coexist before 416 °C, and pyrite continues precipitating after this temperature (Fig. 10b). The highest pyrite precipitation rate occurs at temperature of 447–416 °C, during which the pyrrhotite and magnetite have the highest consumption rate (Fig. 10b). The initial gold precipitation occurs at 477 °C, 454 °C, 428 °C and 275 °C, which correspond to the Au concentrations of 200 ppb, 100 ppb, 50 ppb and 20 ppb, respectively (Fig. 10b). The auriferous fluids with gold concentrations of 200 ppb and 100 ppb experience rapid gold precipitation shortly after gold saturation (Fig. 10b).

The H_2S^0 is the dominated S-bearing aqueous species and shows concentration decrease tendency from 500 °C to 250 °C (Fig. 10c). The HS^- concentration shows a slight fluctuation in the auriferous fluid as cooling. The $logfo_2$ decreases from –23.3 at 500 °C through −26.1 at 450 °C to −29.6 at 400 °C (Fig. 10c). The pH range of the auriferous fluid is 4.65–4.83 at 500–250 °C (Fig. 10d), which is

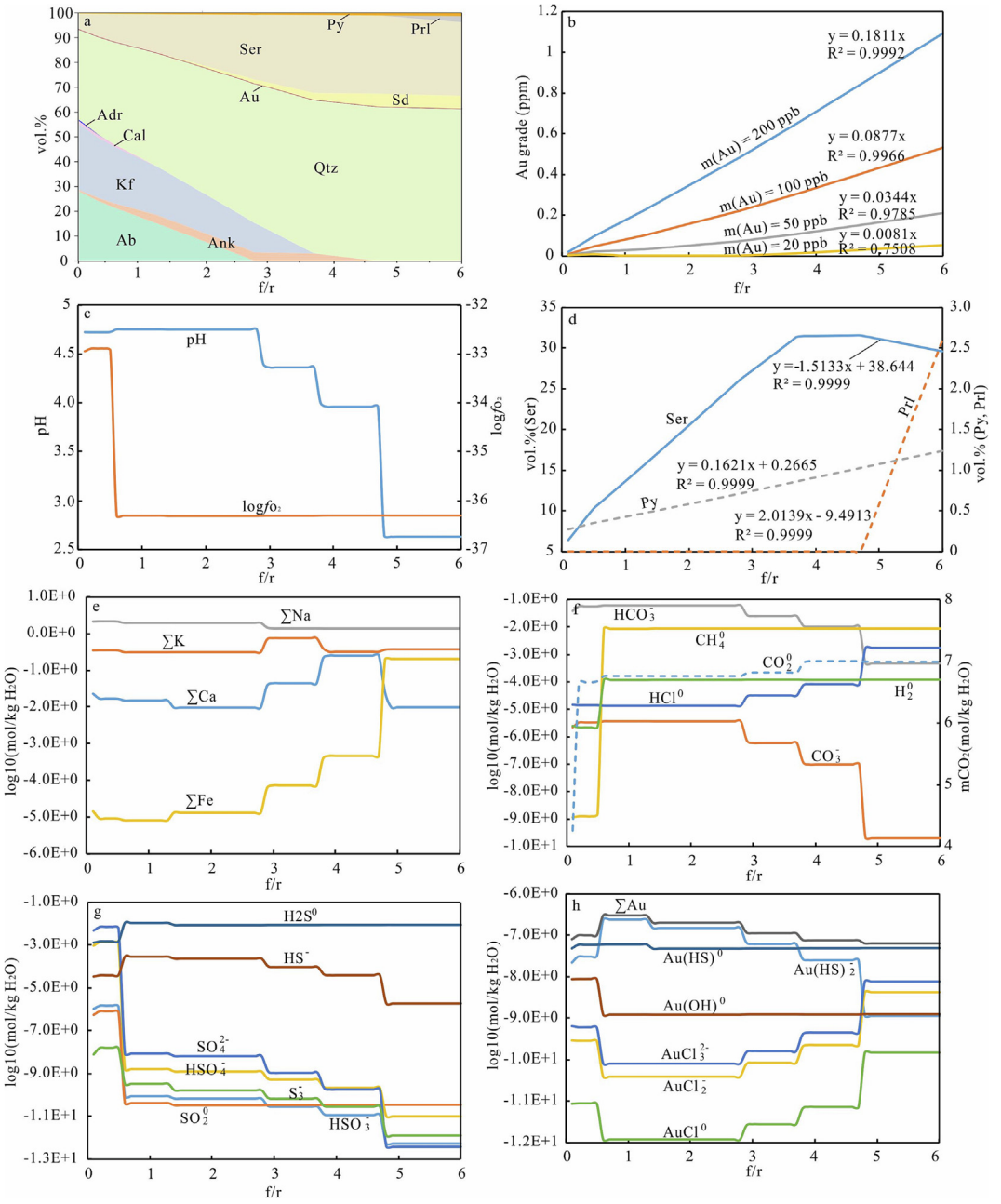

Fig. 9. The flow-through modeling results at 300 °C and 2000 bar. (a) Mineral assemblage. (b) Gold grade. (c) pH and $logfo_2$ of reacted fluids. (d) Volume variations of pyrite, sericite and pyrophyllite. (e)–(h) Concentration variations of aqueous species in reacted fluids. Abbreviations: Adr = anhydrite, Prl = pyrophyllite.

relatively constant due to the feldspars buffering (Fig. 10a). The dominated Au-bearing complexes are the $AuCl_2^-$ and $AuCl_3^{2-}$ at 500–456 °C (Fig. 10d). The $Au(HS)_2^-$ and $Au(HS)^0$ become predominant Au-bearing complexes at 456–411 °C. And the $Au(HS)_2^-$ dominates the gold solubility after 411 °C.

(2) Cooling modeling for the 40th fluid-rock reaction process Alkali feldspar solid solution and anorthite experience reaction to form plagioclase at 456 °C (Fig. 11a). Plagioclase eventually disappears at 418 °C without albite and K-feldspar crystallization (Fig. 11a). Ankerite and siderite begin to precipitate at 451 °C and 434 °C, respectively (Fig. 11a). Pyrrhotite and magnetite coexist before 418 °C, and pyrite continues precipitating after this temperature (Fig. 11b). The highest precipitation rate for pyrite occurs at temperature of 456–418 °C with the highest consumption rate of pyrrhotite and magnetite (Fig. 11b). The initial gold precipitation temperatures are 478 °C, 455 °C, 427 °C and 339 °C, which correspond to the initial Au concentrations of 200 ppb, 100 ppb, 50 ppb and 20 ppb, respectively (Fig. 11b). The auriferous fluids with gold concentrations of 200 ppb and 100 ppb experience rapid gold precipitation shortly after Au saturation (Fig. 11b).

The H_2S^0 is the dominated S-bearing aqueous species and shows concentration decrease tendency from 500 °C to 250 °C (Fig. 11c). The HS^- concentration shows a slight decrease as cooling. The $logfo_2$ decreases from −23.8 at 500 °C through −26.1 at 450 °C to −29.6 at 400 °C (Fig. 11c). The pH of the auriferous fluid decreases from 4.6 to 3.7 during cooling from 500 °C to 250 °C (Fig. 11d). The dominated Au complexes are the $AuCl_2^-$ and $AuCl_3^{2-}$ at 500–459 °C, and the $Au(HS)^0$ and $Au(HS)_2^-$ become the main Au-bearing complexes after 459 °C (Fig. 11d).

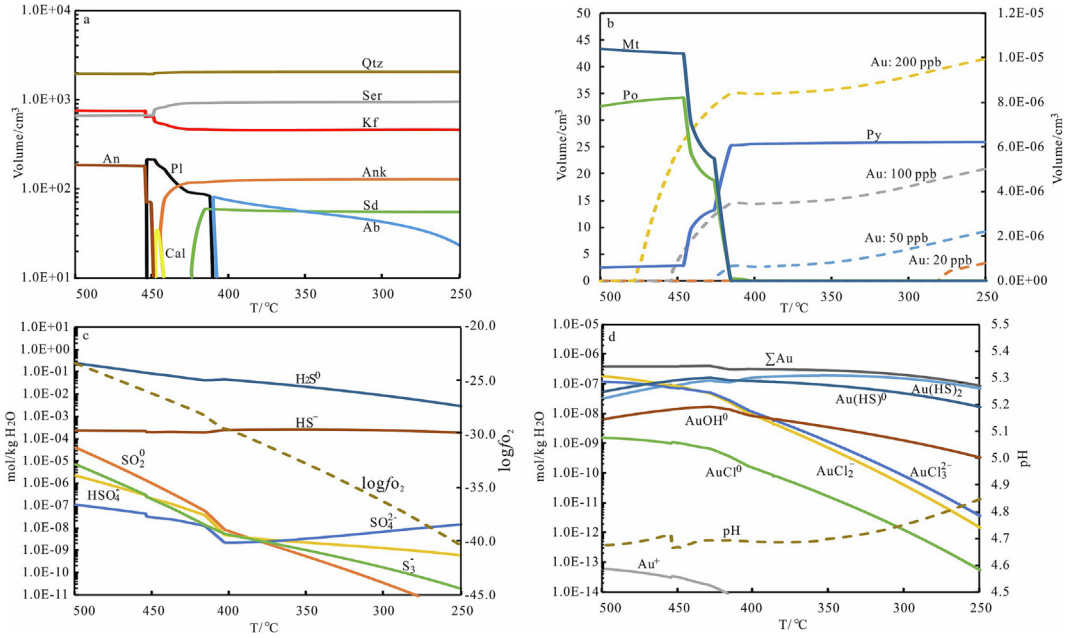

Fig. 10. The cooling modeling results for the 27th fluid-rock reaction process (Fig. 8b). (a) Mineral assemblage. (b) Volume variations of magnetite, pyrrhotite and pyrite (left Y-axis), and gold volume variations in reacted rock cells at different initial Au concentrations (right Y-axis). (c) Concentration variations of S-bearing aqueous species in reacted fluids. (d) Concentration variations of Au-bearing complexes in the reacted fluid with initial Au concentration of 50 ppb (left Y-axis), and pH variation (right Y-axis). Abbreviations: An = anorthite, Mt = magnetite, Po = pyrrhotite.

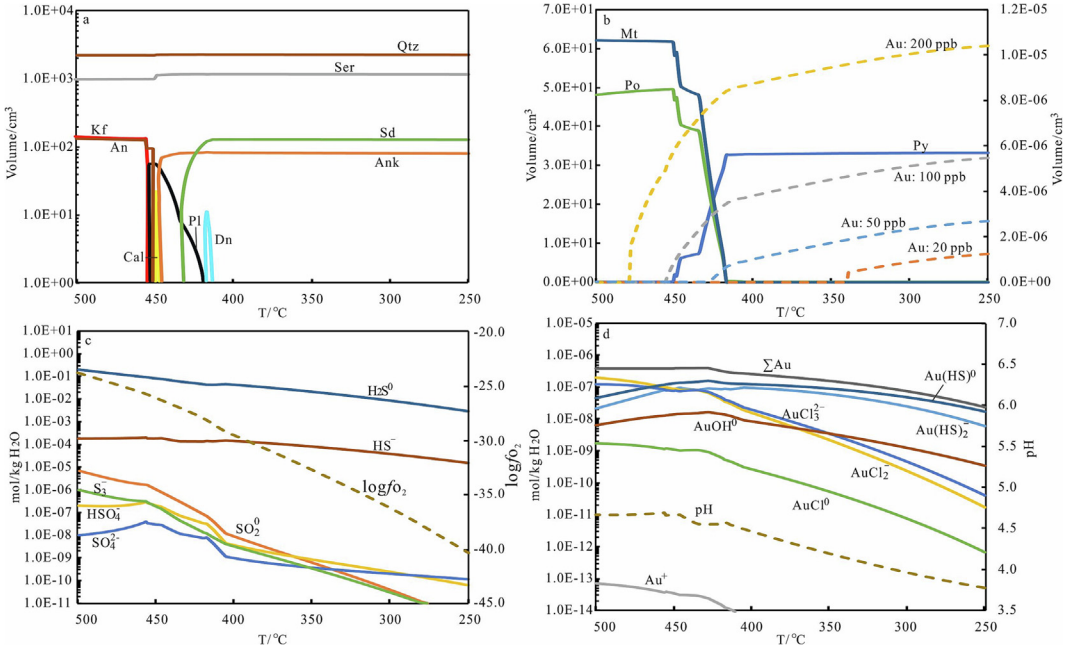

Fig. 11. The cooling modeling results for the 40th fluid-rock reaction process (Fig. 8c). (a) Mineral assemblage. (b) Volume variations of magnetite, pyrrhotite and pyrite (left Y-axis), and gold volume variations in reacted rock cells at different initial Au concentrations (right Y-axis). (c) Concentration variations of S-bearing aqueous species in reacted fluids. (d) Concentration variations of Au-bearing complexes in the reacted fluid with initial Au concentration of 50 ppb (left Y-axis), and pH variation (right Y-axis). Dn = daphnite.

(3) Cooling modeling for the initial auriferous fluid Feldspars, pyrrhotite, siderite and ankerite cannot crystallize in this modeling (Fig. 12a). Sericite and pyrophyllite are stable at 466–371 °C and 372–358 °C, respectively (Fig. 12a). Quartz begins to precipitate from the auriferous fluid at 447 °C. Magnetite exists before 457 °C and transforms to pyrite after this temperature (Fig. 12b). Pyrite occurs rapid precipitation after ~400 °C. The initial gold precipitation temperatures are 440 °C, 384 °C, 310 °C and 271 °C for the Au concentrations of 200 ppb, 100 ppb, 50 ppb and 20 ppb, respectively (Fig. 12b). The auriferous fluid with gold concentration of 200 ppb experiences rapid gold precipitation shortly after gold saturation (Fig. 12b).

The H_2S^0 concentration slightly increases from 500 °C to 463 °C, and decrease as cooling from 463 to 250 °C (Fig. 12c). The HS^- con-

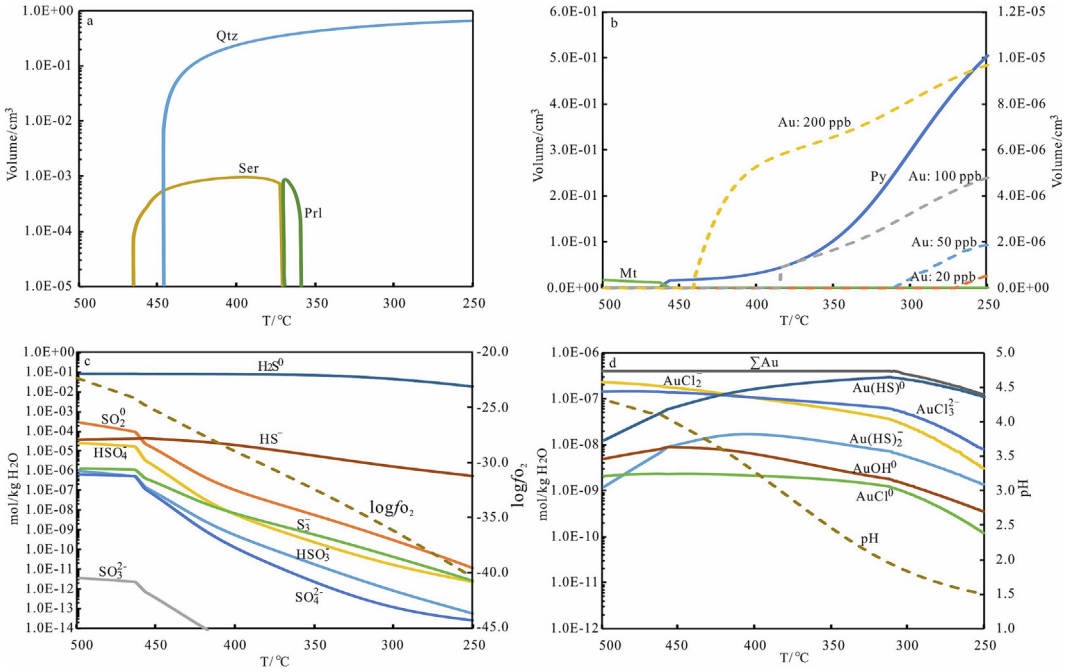

Fig. 12. The cooling modeling results for the initial auriferous fluid (Fig. 8d). (a) Mineral assemblage. (b) Volume variations of magnetite and pyrite (left Y-axis), and gold volume variations in reacted rock cells at different initial Au concentrations (right Y-axis). (c) Concentration variations of S-bearing aqueous species in reacted fluids. (d) Concentration variations of Au-bearing complexes in the reacted fluid with initial Au concentration of 50 ppb (left Y-axis), and pH variation (right Y-axis).

centration slightly increases from 500 °C to 459 °C due to the SO_2^0 reduction, and decreases as cooling from 459 °C to 250 °C (Fig. 12c). The $logfo_2$ decreases from −22.4 at 500 °C through −25.3 at 450 °C to −29.0 at 400 °C (Fig. 12c). The pH of the auriferous fluid decreases from 4.3 to 1.5 when cooling from 500 °C to 250 °C (Fig. 12d). The dominated Au complexes are $AuCl_2^-$ and $AuCl_3^{2-}$ at 500–417 °C, and the $Au(HS)^0$ becomes the main Au-bearing complex after 417 °C (Fig. 12d).

6. Discussion

6.1. Gold transport and precipitation

Gold transport and precipitation affect the gold enrichment to form orebody. The cooling modeling projects for the 27th and 40th fluid-rock reaction processes show the similar gold transport and precipitation processes for the given initial gold concentrations (Fig. 10b–d; Fig. 11b–d). This is related to the changes of Au-bearing complexes and total sulfur concentration in the auriferous fluid. The main gold complex is the $AuCl_2^-$ in acidic saline fluids in 500–460 °C and the Au-S complexes dominate gold solubility when temperature is below ~460 °C (Fig. 9h, 10d, 11d; Stefánsson and Seward, 2004; Williams-Jones et al., 2009; Pokrovski et al., 2014). In this case, pyrite precipitation at <460 °C can remarkably decrease gold solubility and hinder gold long-range transport to lower-temperature environment.

The cooling modeling of the initial auriferous fluids shows that gold has the lower initial precipitation temperatures than those in the cooling modeling results of the 27th and 40th fluid-rock reaction processes at the same initial Au concentrations (Fig. 10b, 11b, 12b). These differences should be controlled by the oxidizability and total sulfur concentration of auriferous fluids. The alone initial auriferous fluid cooling modeling shows the higher $logfo_2$ than that of the auriferous fluids in the 27th and 40th cooling with fluid-rock interaction modeling at the same temperature at >400 °C (Fig. 10c, 11c, 12c). This is because the $logfo_2$ in the auriferous fluid of the former cooling modeling is only buffered by magnetite, but the $logfo_2$ in the auriferous fluids of the latter two modeling projects are buffered by magnetite-pyrrhotite-(pyrite) (Fig. 10b, 11b, 12b). The higher $logfo_2$ at >400 °C should enhance the Au-Cl complexes stability and suppress the gold precipitation, which postpones the gold precipitation to lower temperature (Fig. 10b, 11b, 12b; Zhu et al., 2011; Williams-Jones et al., 2009; Pokrovski et al., 2014). In addition, the cooling modeling for the initial auriferous fluids shows the pH rapidly decreases as cooling due to the lack of feldspars buffering (Fig. 12d). The lower pH can hinder pyrite precipitation (R1 according to the modeling results),

$$Fe^{2+} + 2H_2S^0 + 0.5O_{2(aq)} = FeS_{2(pyrite)} + H_2O_{(l)} + 2H^+ \quad (R1).$$

which also delays the gold precipitation to lower temperature (Fig. 10b, 11b, 12b). Therefore, the high oxidizability, low pH and high total sulfur concentration should account for the long-range gold transfer to lower-temperature environment.

In the Jiaojia goldfield, the typical wallrock alteration zonation with intense fluid-rock interaction had given some important effects on the gold precipitation and enrichment during cooling and decompression processes (Fig. 2b–c; Fig. 4a–f; Fig. 5a–f). The auriferous fluid would acquire higher pH by the buffering of feldspars or sericite during fluid-rock interaction processes (Fig. 9d, 10d, 11d), which was beneficial for the high-efficiency precipitations of pyrite and gold during the fluid cooling from >390 °C and decompression at the mineralization sites of the Jiaojia goldfield (Fig. 4d–f; Fig. 5g–i; Wei et al., 2019; Hu et al., 2021).

6.2. The ore fluid to rock mass ratios for the pyrite-sericite-quartz alteration

The amount of gold enrichment during pyrite-sericite-quartz alteration process should be restricted by the ore fluid amount during fluid-rock interaction, in which the ore fluid amount is further limited by the mineral assemblage with specific f/r values (Heinrich, 2005; Dolejš and Wagner, 2008; Mernagh and Bierlein, 2008; Reed et al., 2013). Therefore, the f/r values with specific

alteration mineral assemblage limit the gold grade increase in the alteration zones. The fluid-rock interaction modeling for the pyrite-sericite-quartz alteration process in the Jiaojia goldfield can give a f/r constraint between the alteration mineral assemblages and gold enrichment. Fluid-rock interaction with cooling controls albite crystallization with subsequent preferential stronger sericite-quartz alteration than K-feldspar (Figs. 9a, 10a, 11a). The causes are that the water dielectric constant increase as cooling favors the dissociation of HCl^0 and $H_2CO_3^0$, and the activated H^+ will preferentially accelerate the albite alteration to sericite and quartz (Dolejš and Wagner, 2008; Williams-Jones et al., 2009; Li et al., 2013a). These simulation results are consistent with that the albite crystallization with subsequent preferential alteration than K-feldspar occurs in the weak pyrite-sericite-quartz alteration stockworks of the K-feldspar alteration zone (Figs. 4a, 5a). The ankerite exhaustion leads to the pH plunge from 3.96 to 2.63 and siderite dissolution when the f/r is above 4.8 (Fig. 9c) due to the lack of CO_3^{2-} replenishment from ankerite to associate with H^+ (R2 and R3; Fig. 9a). The large pH decrease facilitates pyrophyllite crystallization by consuming muscovite, quartz and H^+ (R4; Fig. 9d).

$CaFe(CO_3)_{2(ankerite)} + H^+ = Ca^{2+} + FeCO_{3(siderite)} + HCO_3^-$ (R2).

$FeCO_{3(siderite)} + H^+ = Fe^{2+} + HCO_3^-$ (R3).

$KAl_2(AlSi_3)O_{10}(OH)_{2(sericite)} + SiO_{2(s)} + 2H^+ = Al_2Si_4O_{10}(OH)_{2(pyrophyllite)} + K^+ + H_2AlO_2^+$ (R4).

Therefore, ankerite can buffer the pH of auriferous fluids to prevent sericite alteration to pyrophyllite at f/r of 3.8–4.8 (Fig. 9a, d). The observations of ankerite and siderite but no pyrophyllite in the pyrite-sericite-quartz alteration zone support the f/r of 3.8–4.8 for this alteration in the Jiaojia goldfield (Fig. 4f, 6a; Fig. S1, S2). The thermodynamically predicted volume fractions of quartz (65.7%), sericite (33.2%) and pyrite (1.1%) for the pyrite-sericite-quartz alteration rock at f/r 4.8 approach the calculated volume fractions of quartz (57.5%), sericite (39.2%) and pyrite (3.3%, approximate calculation from the analytical Fe content) from the major elements results of the pyrite-sericite-quartz alteration rock (Fig. 9a; Fig. S4). All these consistencies indicate a f/r range of 3.8–4.8 is reasonable for the transformation from K-feldspar alteration to pyrite-sericite-quartz alteration in the Jiaojia goldfield.

It is noteworthy the temperature and pressure fluctuations should have effects on the f/r values of minerals disappearance (Dolejš and Wagner, 2008; Mernagh and Bierlein, 2008; Pokrovski et al., 2014; Xu et al., 2016). The pyrite-sericite-quartz alteration stage has a main fluid inclusion homogenization temperature of ~350–250 °C in the Jiaojia goldfield (Yang et al., 2017; Wei et al., 2019). Cooling from 350 °C to 250 °C shows a little effect on the dissolution of feldspars, ankerite and siderite (Figs. 10a, 11a), which suggests the f/r values for the minerals disappearance experiences limit variations in this temperature range. The pressure mainly ranging in ~500–2000 bar could result in fluid immiscibility in the Jiaojia goldfield (Yang et al., 2017). The constrained initial auriferous fluid composition (approximate 10 mol.% CO_2, 2.7 mol.% NaCl and 87.3 mol.% H_2O; Table 1) should experience limited fluid immiscibility during the fluid-rock interaction at 500–2000 bar and 300 °C, according to the calculated immiscibility line of H_2O-CO_2-NaCl fluid at 300 °C and 2000 bar (Fig. 2 in Li et al. (2020)). This means the pressure fluctuation at 500 bar to <2000 bar and 300 °C should not produce remarkable f/r deviation for the disappearances of feldspars and carbonates relative to those at 2000 bar and 300 °C. Therefore, the f/r 3.8–4.8 is a reliable estimation although it can be affected by physicochemical conditions fluctuations.

6.3. Gold grade increase during pyrite-sericite-quartz alteration

Four gold grades, ranging in 0.69–0.87 ppm, 0.33–0.42 ppm, 0.13–0.17 ppm and 0.03–0.04 ppm, are calculated out for the pyrite-sericite-quartz alteration at f/r of 3.8–4.8, when using the initial auriferous fluids with gold concentrations of 200 ppb, 100 ppb, 50 ppb and 20 ppb for flow-through modeling, respectively (Fig. 9b). The gold grade in the alteration zone is controlled by both the gold solubility and f/r value. The calculated gold solubility results contain some uncertainties due to the possible imprecise thermodynamic model with parameters (Tanger and Helgeson, 1988; Plyasunov and shock, 2001; Pokrovski et al., 2014), and incomplete consideration for all Au-bearing complexes (Mei et al., 2013; Pokrovski et al., 2014; Pokrovski and Dubessy, 2015). The flow-through modeling at 300 °C and 2000 bar is below the critical point of water, which means the predicted dissolutions of the most important aqueous nonelectrolytes H_2S and CO_2 with the parameters of revised HKF model are reliable (Supcrt slop07.-dat; Shock et al., 1989; Plyasunov and Shock, 2001; and references therein). Moreover, a large part of aqueous reduced sulfur can be consumed by pyrite precipitation due to the low pyrite solubility as cooling (total sulfur concentration with <0.01 mol/kg H_2O at 300 °C by pyrite saturation; Kouzmanov and Pokrovski, 2012; Rauchenstein-Martinek et al., 2014). Abundant pyrite with Fe-bearing carbonates and pyrrhotite in the orebodies indicate that the auriferous fluid was enriched in Fe^{2+} with a lot of consumption of aqueous reduced sulfur in the Jiaojia goldfield (Fig. 4d–f; Hu et al., 2020a, b). These mineralization characteristics support the calculated total sulfur concentration of 0.008 mol/kg H_2O after pyrite precipitation in the auriferous fluid (Fig. 9g). The low total sulfur concentration with reduced condition cannot support the stable solutes of polysulfur radical ions (e.g. S_3^-), molecular sulfurs, thiosulfate, polysulfide, and their Au-bearing complexes (e.g. AuHS$(H_2S)^0$, AuS_3 and $Au(HS)S_3^-$) in the Jiaojia goldfield (Fig. 9g; Mei et al., 2013; Pokrovski et al., 2014; Pokrovski and Dubessy, 2015). Therefore, neglecting the unstable Au-bearing complexes cannot significantly affect the gold solubility calculation.

Previous experiment data indicate that the gold solubility can be 40–60 ppb at 300 °C, total sulfur concentration of ~0.03 mol/kg H_2O and acidic conditions (Stefánsson and Seward, 2004). Other fluid-rock modeling results also show that the gold solubility can be low to 10 ppb at 300 °C and pyrite-(pyrrhotite)-(magnetite) saturation conditions (e.g. Mernagh and Bierlein, 2008; Pokrovski et al., 2015; Petrella et al., 2021). These results indicate the calculated gold solubility between $10^{-6.53}$ mol/kg H_2O (~40 ppb in auriferous fluid) and $10^{-7.12}$ mol/kg H_2O (~10 ppb in auriferous fluid) at f/r of 1.0–4.8 and total sulfur concentration of 0.008 mol/kg H_2O should be reliable (Fig. 9h). The gold solubility can be further decreased due to the total sulfur concentration decrease by cooling to <300 °C and decompression with polymetallic sulfides precipitation and fluid immiscibility (Yang et al., 2017; Wei et al., 2019). Therefore, the calculated gold grades at f/r of 3.8–4.8 can be used as a robust reference to reveal the gold enrichment processes for the Jiaojia goldfield.

6.4. Fracture-induced fluid flow for gold transport and enrichment

The single fluid-rock interaction obviously cannot elevate the gold grade to >1 ppm in the Jiaojia goldfield, due to the f/r limit and high gold saturation temperature with dispersive precipitation along migration conduits. Fracture-induced fluid flow coupled with fluid-rock interaction should be considered to optimize the gold mineralization processes given the Jiaodong gold deposits are controlled by regional-scale fault zones (Goldfarb and Santosh, 2014; Deng et al., 2019; Fan et al., 2021). Intense structure activities

(e.g., shearing and earthquake) can lead to pressure plunge with rapid migration of auriferous fluid along high-permeability zone (Micklethwaite and Cox, 2006; Weatherley and Henley, 2013). These kinds of structure activities could weaken heat dissipation and fluid-rock interaction and effectively focus the auriferous fluid into the shallow mineralization sites in the Jiaojia goldfield (Wang et al., 2016; Deng et al., 2019). The stable alteration zonation pattern of lateral direction and the same evolution of ore fluid at different levels could extend to −2855 m below the ground in the Jiaojia goldfield (Table S1), and to −3000 – −000 m below the ground at other Jiaodong gold deposits (Li et al., 2013a, 2015; Wen et al., 2016). The trap temperature in the early mineralization stage can be >400 °C, local to 545 °C, at the Jiaojia and Sanshandao gold deposits (Fan et al., 2003; Wen et al., 2016; Wei et al., 2019). These characteristics support the high-temperature auriferous fluid had experienced rapid transport and subsequent uniform evolution at different levels of mineralization sites during synchronous structure activities. The high temperature with weak and non-equilibrium fluid-rock interaction allows high gold solubility preserved in ore fluid, which avoids dispersive gold precipitation and focuses gold into optimal sites.

Two important aspects in the fracture-induced fluid flow coupled with fluid-rock interaction should be taken into account for gold enrichment in the Jiaojia goldfield. The first is the gold concentration in the initial auriferous fluid. The initial gold concentration of >200 ppb should be easy to form the gold orebodies with >1 ppm by fracture-induced fluid flow with simple fluid-rock interaction (Fig. 9b). The metasomatic lithospheric mantle-derived mafic magmas of 130–120 Ma from the Jiaodong gold province and other area of the eastern NCC margin have 0.4–4.3 ppb (mean 2.2 ppb) Au (Wang et al., 2020, 2022a). The magmatic hydrothermal processes can produce a gold-rich fluid with >200 ppb for the Jiaodong gold deposits combining with the gold partition coefficient of ~10–100 between Cl-(S)-bearing aqueous fluid and silicate melts (Simon et al., 2007). However, whether the magmatic hydrothermal processes for transporting the mantle-derived hydrous volatiles to form the Jiaodong gold deposits (e.g. Zhu et al., 2015; Wang et al., 2020, 2022a) waits further verification. Wang et al. (2022b) have carried out the composition analysis of individual fluid inclusion in quartz veins of the Linglong gold deposit with the LA-ICP-MS instrument, but all the gold concentration data are below the detected limit, which might be limited by sample choice or analytical method. Therefore, acquiring the reliable gold concentration in the auriferous fluid is critical to understand the gold enrichment for the Jiaodong gold province.

Secondly, gold colloids have been suggested to play an important role in forming giant gold deposits with high grade (Saunders and Schoenly, 1995; Petrella et al., 2020; McLeish et al., 2021). Rapid pyrite saturation can induce extremely high degrees of gold supersaturation that are beneficial for the colloidal gold particles formation (Saunders and Schoenly, 1995; McLeish et al., 2021). The pyrite rapid precipitation should be testified by the 60–95 vol% fine-grained pyrite in the ore veinlets of the Jiaojia goldfield. The colloids transport is also implied by the gold nanoparticles reported in the pyrite grains of the Xincheng gold deposit in the Jiaojia fault zone (Yang et al., 2016). Therefore, the gold colloids might be re-transported from the gold saturation sites into the optimal mineralization sites and precipitate as visible gold particles by fracture-induced fluid flow and focusing. Moreover, the auriferous fluid can acquire rapid local equilibrium with silicate minerals in the mineralization sites at above 300 °C (Dolejš and Wagner, 2008). This means the reacted fluid with re-migration could not alter the mineral assemblage of other mineralization sites that had equilibrated with the same reacted fluid. In these cases, the cumulative gold from 1 to 6 pyrite-sericite-quartz alteration rock cells can be re-migrated into a pyrite-sericite-quartz alteration rock cell and increase the gold grade to 1–4 ppm for the cell by structure activities and Au colloids, when using the auriferous fluid with Au concentration of 200 ppb for the flow-through modeling. The same gold grade increase for a pyrite-sericite-quartz alteration rock cell needs cumulative gold from 2 to 12, 6–30 and 25–133 pyrite-sericite-quartz alteration rock cells, when using the auriferous fluids with Au concentrations of 100, 50 and 20 ppb for the flow-through modeling, respectively.

The above predicted gold redistribution and aggregation should be the facts considering the distribution characteristics of the gold orebodies at the Jiaojia and other Jiaodong gold deposits (Figs. 1–2). The gold orebodies present as pinch-out and reappearance in the Jiaojia goldfield according to the current gold cutoff grade (Figs. 2–3). The >1 ppm gold orebodies occupy a little part of the pyrite-sericite-quartz alteration zone, in which the alteration sites with 1–4 ppm grade are the main orebodies (Fig. 3c–d). The clustering of gold deposits in the Jiaojia-Xincheng fault zone was controlled by mainshock and subsequent aftershocks with the formation of local high permeability structures (Wang et al., 2016). The Jiaodong gold deposits only clustered into the limited structure sites while the widespread structure activities with large-scale auriferous fluid upwelling occurred along the regional fault zones (Wang et al., 2016; Deng et al., 2019, 2020; Fan et al., 2021). These characteristics suggest the fracture-induced fluid flow redistributed ore fluid in the alteration space of the ore-controlling fault zones, which further elevated the gold grade at the optimal mineralization sites (Figs. 1–2). Therefore, verifying whether the gold colloids formed in the Jiaodong gold deposits is the other important point to understand the gold enrichment processes. The above discussions suggest the fracture-induced fluid flow processes with fluid-rock interaction are the indispensable prerequisites whatever the high gold concentration or the gold colloid assists the gold grade increase to >1 ppm in the Jiaodong gold province.

6.5. The lithospheric mantle volume estimation for the ore fluid source

The Jiaodong gold province formed during the NCC destruction peak time with abundant mantle-derived magmas (Cai et al., 2013; Zhu et al., 2015; Deng et al., 2017, 2020). Previous C–H-O-S-He-Ar-Pb isotopic compositions implicate the metasomatized lithospheric mantle provide the critical ore materials for the Jiaodong gold deposits (Mao et al., 2008; Zhu et al., 2015; Wen et al., 2016; Deng et al., 2020). The $\Delta^{33}S$-$\delta^{34}S$ results from the ore-related pyrite of the Jiaodong gold deposits indicate the subducted slab-derived sulfur and gold that were stored in the metasomatized lithospheric mantle were the important ore material source for the Jiaodong gold province (Qiu et al., 2023). The calculation of the metasomatized lithospheric mantle volume for the Au resources of the Jiaodong gold province just depends on the gold content in the metasomatized lithospheric mantle without abnormal Au enrichment (Wang et al., 2022a), which ignores whether the ore fluid derived from this calculated mantle volume can result in the synchronous wallrock alteration and giant Au mineralization. Therefore, the link between the metasomatized lithospheric mantle and shallow alteration-mineralization processes still keeps ambiguous. The proposed auriferous fluid transport and gold enrichment processes in combination with the alteration-mineralization characteristics of the Jiaodong gold province can provide the suitable parameters to quantify the above question. The No. I orebody of the Jiaojia gold deposit has a volume of 1.45×10^7 m^3 (960 m × 1370 m × 11 m) and an average gold grade of ~4 ppm (Table S1; Song et al., 2010). The cumulative gold from 24 pyrite-sericite-quartz alteration rock cells (the grade is 0.17 ppm in the cells if the gold has precipitated) is needed to refocus by colloids and increase the gold grade to 4 ppm for a pyrite-

sericite-quartz alteration rock cell, according to the flow-through modeling for the initial auriferous fluid with 50 ppb Au at f/r of 4.8 (Fig. 9b). This means the No. I orebody formation needs 5.00×10^{15} g reacted auriferous fluid from 24 pyrite-sericite-quartz alteration rock cells with a total rock volume of 3.47×10^{8} m^3 (i.e. 1.04×10^{15} g assuming 3 g/cm^3). Two hundred tonnes gold can precipitate from 5.00×10^{15} g ore fluid when the fluid contains 50 ppb Au with the calculated gold precipitation efficiency of 80% for this Au concentration (Fig. 9h). The calculated gold precipitation mass approaches the real 205 tonnes Au in the No. I orebody (Song et al., 2010).

The 5000 tonnes gold resources in the Jiaodong gold province should equal to 25 times of the gold reserves of the No. I orebody. At the same calculation conditions as that for the No. I orebody, the cumulative gold from 600 pyrite-sericite-quartz alteration rock cells is needed to refocus and increase the gold grade to 4 ppm for 25 pyrite-sericite-quartz alteration rock cells. Similarly, the ore fluid mass is 1.25×10^{17} g for this gold province. The H_2O content of the lithospheric mantle under the eastern NCC is estimated to be 1000–7000 ppm (Xia et al., 2013). The lithospheric mantle mass for the initial ore fluid source of the Jiaodong gold province is 1.25×10^{20} g assuming 1000 ppm H_2O release from the mantle by direct devolatilization or magmatic-hydrothermal evolutions. The rock volume corresponds to 3.79×10^{4} km^3 assuming the density of 3.3 g/cm^3. Therefore, a metasomatized lithospheric mantle volume with 100 km long × 100 km wide × 3.79 km thick can provide the required ore fluid amount and 5000 tonnes Au for the Jiaodong gold province according to the estimations from the above calculations and Wang et al. (2022a). In the same calculation way, a metasomatized lithospheric mantle volume with 100 km long × 100 km wide × 0.80 km thick can provide the required ore fluid and Au for the gold province when the Au concentration of 200 ppb with corresponding 95% gold precipitation efficiency is set for the initial auriferous fluid. The required thickness of such H_2O-rich lithospheric mantle is easy to achieve because the eastern NCC had experienced intensive metasomatism and decratonization before 120 Ma (Xia et al., 2013; Zhu et al., 2015; Wu et al., 2019).

6.6. Implications for the links between metasomatized mantle and giant gold mineralization

Previous studies propose that the metasomatized lithospheric mantle with abundant hydrous volatiles should be the first order to control the giant gold deposits formation (Griffin et al., 2013; Groves et al., 2019; Deng et al., 2020; Wang et al., 2022a). Here the Jiaojia goldfield in the world-class Jiaodong Au province can give an excellent case to portray the auriferous fluid transport and gold enrichment pictures for the giant Au mineralization that is related to the metasomatized lithospheric mantle. The asthenospheric upwelling and lithospheric thinning beneath the eastern NCC (Wu et al., 2019) facilitate the metasomatized lithospheric mantle to produce Au-bearing fluid storage by devolatilization and subsequent evolutions beneath the Jiaodong Peninsula (Fig. 13; Mao et al., 2008; Deng et al., 2020; Wang et al., 2022a). The *trans*-lithospheric faults reactivated with synchronous earthquakes during the gold mineralization period (Wang et al., 2016; Deng et al., 2019). The extended period of aftershocks sustained longer-lived, fracture-enhanced permeability, which could open

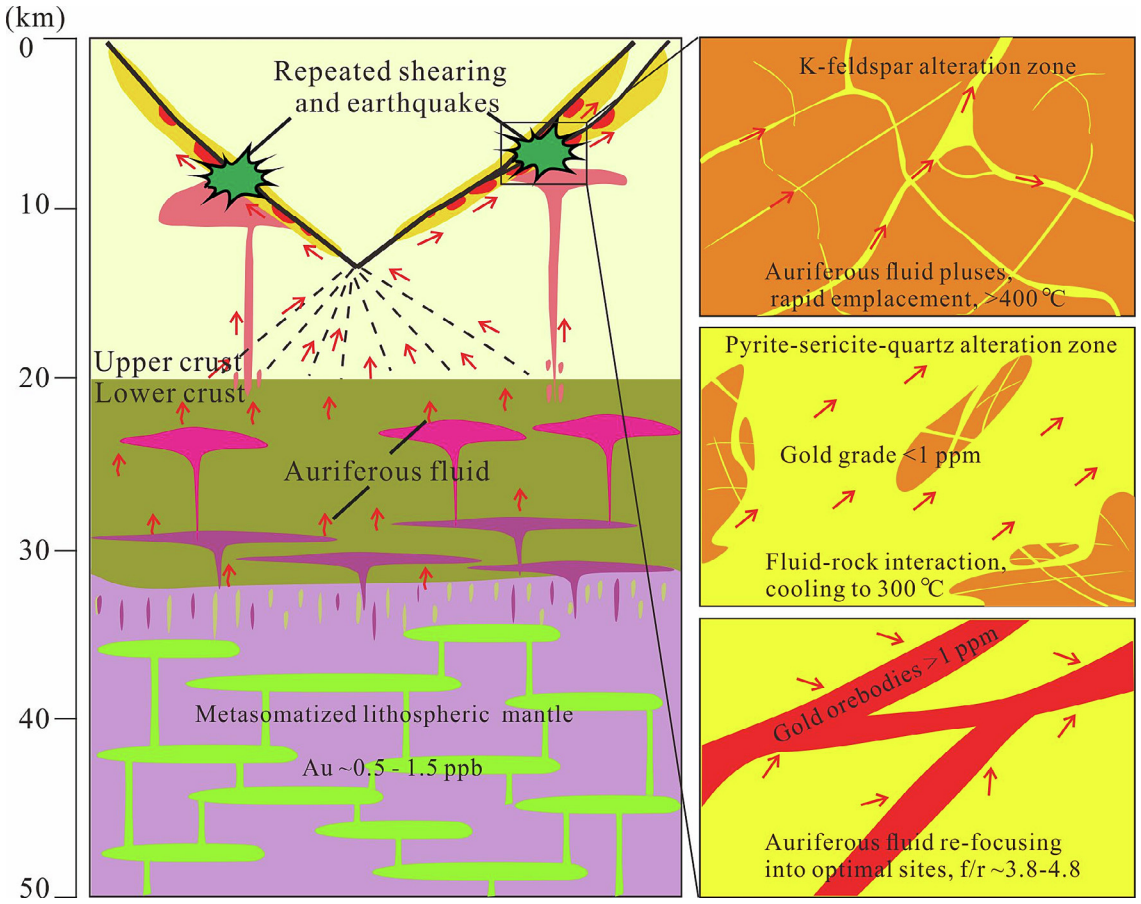

Fig. 13. Fracture-induced fluid flow coupled with fluid-rock interaction processes for the Jiaojia goldfield, providing a critical link between the metasomatized mantle without abnormal Au enrichment and giant gold mineralization. The gold content in the mantle is referenced from Wang et al. (2022a).

the ore fluid migration channels that tapped into the deep fluid storage, induce pulsing high fluid fluxes, and localize the fluids into the shallow fault occurrence change and fault cross sites (Micklethwaite and Cox, 2006; Wang et al., 2016). The auriferous fluid could keep high temperature (>400 °C) before it was pulsed into mineralization sites. Rapid transport of auriferous fluid avoided large heat dissipation and intense fluid-rock interaction with wallrocks along migration channels. These conditions can facilitate the long-range gold transfer. The auriferous fluid could rapidly exchange heat and elements with low-temperature and structure-fractured wallrocks in the mineralization sites. In these cases, the gold supersaturation was induced by rapid total sulfur concentration decrease, which was beneficial for the preliminary gold nucleation to form colloids (McLeish et al., 2021).

About 38–48 effective aftershocks with auriferous fluid pulses can account for the transformation from K-feldspar alteration to pyrite-sericite-quartz alteration assuming the instantaneous f/r value 0.1 for every pulse. This is easily acquired because the main-shock can be followed by thousands of aftershocks that last >30 days to decades (Miller et al., 2004; Micklethwaite and Cox, 2006). The >1 ppm Au grade enrichment in the pyrite-sericite-quartz alteration zone needs either the high Au concentration in the initial auriferous fluid or the Au colloids formation in the reacted fluid. In fact, these two conditions are easy to acquire in the hydrothermal fluid evolution processes. The gold solubility in the S-, C-, Cl-bearing fluids can be higher than 200 ppb due to the more stable Au-Cl and Au-polysulfur radical ions complexes at >450 °C (Figs. 10–12; Ulrich et al., 1999; Heinrich, 2005; Mei et al., 2013; Pokrovski et al., 2015). More and more researches reveal that the gold suspensions are not rare phenomenon in the mesothermal fluids, and the rapid gold supersaturation with appropriate preservation can maintain the gold colloids stability (Saunders and Schoenly, 1995; Liu et al., 2019; Petrella et al., 2020; McLeish et al., 2021). The suspended gold nanoparticles in the reacted fluids can be further refocused into the optimal mineralization sites from ambient pyrite-sericite-quartz alteration zone due to structure activities (Fig. 13). Therefore, combining with the typical case of the Jiaojia goldfield, the auriferous fluids that are initially derived from the metasomatized lithospheric mantle (direct devolatilization or magmatic hydrothermal evolution) can easily form the giant gold deposits by fracture-induced fluid flow coupled with fluid-rock interaction. A link between the metasomatized lithospheric mantle without abnormal Au enrichment and shallow alteration-mineralization processes has been proposed (Fig. 13).

7. Conclusions

The transformation of Au-Cl complexes to Au-S complexes with total sulfur concentration decrease after ~460 °C can trigger the fastest gold saturation during fluid-rock interaction with cooling, which hinders gold precipitation to lower ambient temperature. The lower pH can maintain higher total sulfur concentration and the higher oxidizability can stabilizes the Au-Cl complexes, both of which can postpone the gold precipitation to lower-temperature environment and be beneficial for long-range gold transport. The alteration-mineralization characteristics of the Jiaojia goldfield support the high-temperature auriferous fluid had experienced rapid emplacement and subsequent uniform evolutions at different levels of mineralization sites. These processes resulted in the high temperature with weak and non-equilibrium fluid-rock interaction during ore fluid transport, which could allow high gold solubility preserved in ore fluid and focus gold into optimal sites. Then the auriferous fluid would acquire higher pH by the full buffering of feldspars or sericite, which was beneficial for the high-efficiency precipitations of pyrite and gold at mineralization sites. The flow-through modeling indicates a f/r of 3.8–4.8 for the transformation from K-feldspar alteration to pyrite-sericite-quartz alteration in the Jiaojia goldfield. The gold grade is only increased to 0.69–0.87 ppm in the pyrite-sericite-quartz alteration zone at f/r range of 3.8–4.8, when the initial Au concentrations is set as 200 ppb. Therefore, the fracture-induced fluid flow processes with fluid-rock interaction are the indispensable prerequisites whatever the high gold concentration or the gold colloid, both of which need further verification, assists the gold grade increase to >1 ppm in the pyrite-sericite-quartz alteration zone. The modeling results combining with the metasomatized lithospheric mantle volume estimation for the ore fluid source provide a link between the mantle without abnormal Au enrichment and shallow alteration-mineralization processes.

Declaration of Competing Interest

The authors declare that they have no known competing financial interests or personal relationships that could have appeared to influence the work reported in this paper.

Acknowledgments

We are indebted to Rong-Xin Zhao from Shandong Gold Group Co., Ltd for their kindly helps during field works. Drs. Ya-Chun Cai, Bo-Jie Wen, Hong-Wei Peng and Yong-Wen Zhang are greatly thanked for their field sampling assistance. Drs. Xin Yan and Shao-Hua Dong are acknowledged for their generous helps during BSE imaging. We also thank He-Ping Zhu, Ding-Shuai Xue, Liang-Liang Huang, Ying-Hua Chen and Jian-Guo Li for their generous assistances in fluid inclusion bulk composition analysis, whole-rock geochemistry, Raman mineral identification and EPMA analysis. We are grateful to two anonymous reviewers and Associate Editor Dr. Richard Palin for their constructive feedback that helped to improve the manuscript. This study is financially supported by the National Key Research and Development Program of China (Grant No. 2018YFA0702603) and National Natural Science Foundation of China (41873048). It is also supported by the West Light Foundation of The Chinese Academy of Sciences (Grant No. xbzg-zdsys-202108).

Appendix A. Supplementary material

Supplementary data to this article can be found online at https://doi.org/10.1016/j.gr.2023.07.015.

References

Cai, Y.C., Fan, H.R., Santosh, M., Liu, X., Hu, F.F., Yang, K.F., Lan, T.G., Yang, Y.H., Liu, Y. S., 2013. Evolution of the lithospheric mantle beneath the southeastern North China Craton: Constraints from mafic dikes in the Jiaobei terrain. Gondw. Res. 24, 601–621.

Cai, Y.C., Fan, H.R., Santosh, M., Hu, F.F., Yang, K.F., Li, X.H., 2018. Decratonic gold mineralization: Evidence from the Shangzhuang gold deposit, eastern North China Craton. Gondw. Res. 54, 1–22.

Chen, J., Du, L.J., Yang, R.D., Zhou, M.F., Lai, C.-K., Huang, Z.L., 2022. New insights into the source of gold in the Youjiang basin. SW China. GSA Bulletin. 135, 955–966.

Choi, E., Fiorentini, M.L., Hughes, H.S.R., Giuliani, A., 2020. Platinum-group element and Au geochemistry of Late Archean to Proterozoic calc-alkaline and alkaline magmas in the Yilgarn Craton. Western Australia. Lithos 374–375, 105716.

Deng, J., Liu, X.F., Wang, Q.F., Dilek, Y., Liang, Y.Y., 2017. Isotopic characterization and petrogenetic modeling of Early Cretaceous mafic diking—Lithospheric extension in the North China craton, eastern Asia. The Geological Society of America 129, 1379–1407.

Deng, J., Yang, L.Q., Li, R.H., Groves, D.I., Santosh, M., Wang, Z.L., Sai, S.X., Wang, S.R., 2019. Regional structural control on the distribution of world-class gold deposits: An overview from the Giant Jiaodong Gold Province. China. Geol. J. 54, 378–391.

Deng, J., Yang, L.Q., Groves, D.I., Zhang, L., Qiu, K.F., Wang, Q.F., 2020. An integrated mineral system model for the gold deposits of the giant Jiaodong province, eastern China. Earth Sci. Rev. 208, 103274.
Dolejš, D., Wagner, T., 2008. Thermodynamic modeling of non-ideal mineral–fluid equilibria in the system Si–Al–Fe–Mg–Ca–Na–K–H–O–Cl at elevated temperatures and pressures: Implications for hydrothermal mass transfer in granitic rocks. Geochim. Cosmochim. Acta 72, 526–553.
Evans, K.A., Phillips, G.N., Powell, R., 2006. Rock-Buffering of Auriferous Fluids in Altered Rocks Associated with the Golden Mile-Style Mineralization, Kalgoorlie Gold Field, Western Australia. Econ. Geol. 101, 805–817.
Fan, H.R., Zhai, M.G., Xie, Y.H., Yang, J.H., 2003. Ore-forming fluids associated with granite-hosted gold mineralization at the Sanshandao deposit, Jiaodong gold province. China. Miner. Deposita 38, 739–750.
Fan, H.R., Lan, T.G., Li, X.H., Santosh, M., Yang, K.F., Hu, F.F., Feng, K., Hu, H.L., Peng, H. W., Zhang, Y.W., 2021. Conditions and processes leading to large-scale gold deposition in the Jiaodong province, eastern China. Sci. China Earth Sci. 64, 1504–1523.
Goldfarb, R.J., Groves, D.I., 2015. Orogenic gold: Common or evolving fluid and metal sources through time. Lithos 233, 2–26.
Goldfarb, R.J., Santosh, M., 2014. The dilemma of the Jiaodong gold deposits: Are they unique? Geosci. Front. 5, 139–153.
Goldfarb, R.J., Groves, D.I., Gardoll, S., 2001. Orogenic gold and geologic time: a global synthesis. Ore Geol. Rev. 18, 1–75.
Griffin, W.L., Begg, G.C., O'Reilly, S.Y., 2013. Continental-root control on the genesis of magmatic ore deposits. Nat. Geosci. 6, 905–910.
Groves, D.I., Zhang, L., Santosh, M., 2019. Subduction, mantle metasomatism, and gold: A dynamic and genetic conjunction. GSA Bull. 132, 1419–1426.
Guo, L.N., Zhang, C., Song, Y.Z., Chen, B.H., Zhou, Z., Zhang, B.L., Xu, X.L., Wang, Y.W., 2014. Hydrogen and oxygen isotopes geochemistry of the Wang'ershan gold deposit. Jiaodong. Acta Petrol. Sin. 30, 2481–2494. In Chinese with English abstract.
Gysi, A.P., 2017. Numerical simulations of CO_2 sequestration in basaltic rock formations: challenges for optimizing mineral-fluid reactions. Chim. Pure Appl. 89, 581–596.
Heinrich, C.A., 2005. The physical and chemical evolution of low-salinity magmatic fluids at the porphyry to epithermal transition: a thermodynamic study. Miner. Deposita 39, 864–889.
Heinrich, C.A., Walshe, J.L., Harrold, B.P., 1996. Chemical mass transfer modelling of ore-forming hydrothermal systems: current practise and problems. Ore Geol. Rev. 10, 319–338.
Helgeson, H.C., Kirkham, D.H., Flowers, G.C., 1981. Theoretical prediction of the thermodynamic behavior of aqueous electrolytes at high pressures and temperatures: IV. Calculation of activity coefficients, osmotic coefficients, and apparent molal and standard and relative partial molal properties to 600 °C and 5 kb. Am. J. Sci. 281, 1249–1516.
Holland, T., Powell, R., 2003. Activity–composition relations for phases in petrological calculations: an asymmetric multicomponent formulation. Contrib. Miner. Petrol. 145, 492–501.
Holwell, D.A., Fiorentini, M.L., McDonald, I., Lu, Y.J., Giuliani, A., Smith, D.J., Keith, M., Locmelis, M., 2019. A metasomatized lithospheric mantle control on the metallogenic signature of post-subduction magmatism. Nat. Commun. 10, 3511.
Hronsky, J.M.A., Groves, D.I., Loucks, R.R., Begg, G.C., 2012. A unified model for gold mineralisation in accretionary orogens and implications for regional-scale exploration targeting methods. Miner. Deposita 47, 339–358.
Hu, H.L., Liu, S.L., Fan, H.R., Yang, K.F., Zuo, Y.B., Cai, Y.C., 2020a. Structural Networks Constraints on Alteration and Mineralization Processes in the Jiaojia Gold Deposit, Jiaodong Peninsula. China. J. Earth Sci. 31, 500–513.
Hu, H.L., Fan, H.R., Liu, X., Cai, Y.C., Yang, K.F., Ma, W.D., 2020b. Two-stage gold deposition in response to H_2S loss from a single fluid in the Sizhuang deposit (Jiaodong, China). Ore Geol. Rev. 120, 1–16.
Hu, H.L., Jiang, X.H., Liang, G.Z., Yang, K.F., Fan, H.R., 2021. The Vertical Variation Characteristics of Ore-forming Fluids of the Jiaojia Deposit: Implications for Mineralizing Processes of Gold Deposits in the Jiaodong Peninsula. Bull. Mineral. Petrol. and Geochem. 40, 1345–1356. In Chinese with English abstract.
Jiang, Y.H., Jiang, S.Y., Ling, H.F., Ni, P., 2010. Petrogenesis and tectonic implications of Late Jurassic shoshonitic lamprophyre dikes from the Liaodong Peninsula, NE China. Mineral. Petrol. 100, 127–151.
Kouzmanov, K., Pokrovski, G.S., 2012. Hydrothermal Controls on Metal Distribution in Porphyry Cu(-Mo-Au) Systems. Society of Economic Geologists, Inc. Special Publication 16, 573–618.
Kulik, D.A., Wagner, T., Dmytrieva, S.V., Kosakowski, G., Hingerl, F.F., Chudnenko, K. V., Berner, U.R., 2013. GEM-Selektor geochemical modeling package: revised algorithm and GEMS3K numerical kernel for coupled simulation codes. Comput. Geosci. 17, 1–24.
Li, G.J., Wang, Q.F., ZHu, H.P., Yuan, W.M., Gong, Q.J., 2013b. Fluids inclusion constraints on the origin of the Shiduolong hydrothermal vein-type Mo-Pb-Zn deposit, Qinghai Province. Acta Petrol. Sin. 29, 1377-1391 (In Chinese with English abstract).
Li, X.C., Fan, H.R., Santosh, M., Hu, F.F., Yang, K.F., Lan, T.G., 2013b. Hydrothermal alteration associated with Mesozoic granite-hosted gold mineralization at the Sanshandao deposit, Jiaodong Gold Province. China. Ore Geol. Rev. 53, 403–421.
Li, X.H., Fan, H.R., Hu, F.F., Hollings, P., Yang, K.F., Liu, X., 2019. Linking lithospheric thinning and magmatic evolution of late Jurassic to early cretaceous granitoids in the Jiaobei Terrane, southeastern North China Craton. Lithos 324–325, 280–296.
Li, X.H., Klyukin, Y.I., Steele-MacInnis, M., Fan, H.R., Yang, K.F., Zoheir, B., 2020. Phase equilibria, thermodynamic properties, and solubility of quartz in saline-aqueous-carbonic fluids: Application to orogenic and intrusion-related gold deposits. Geochim. Cosmochim. Acta 283, 201–221.
Li, L., Santosh, M., Li, S.R., 2015. The 'Jiaodong type' gold deposits: Characteristics, origin and prospecting. Ore Geol. Rev. 65, 589–611.
Li, H.J., Wang, Q.F., Yang, L., Dong, C.Y., Weng, W.J., Deng, J., 2022. Alteration and mineralization patterns in orogenic gold deposits: constraints from deposit observation and thermodynamic modeling. Chem. Geol. 607, 121012.
Liu, W.H., Chen, M., Yang, Y., Mei, Y., Etschmann, B., Brugger, J., 2019. Colloidal gold in sulphur and citrate-bearing hydrothermal fluids: An experimental study. Ore Geol. Rev. 114, 103142.
Mao, J.W., Wang, Y.T., Li, H.M., Pirajno, F., Zhang, C.Q., Wang, R.T., 2008. The relationship of mantle-derived fluids to gold metallogenesis in the Jiaodong Peninsula: Evidence from D-O–C–S isotope systematics. Ore Geol. Rev. 33, 361–381.
McLeish, D.F., Williams-Jones, A.E., Vasyukova, O.V., Clark, J.R., Board, W.S., 2021. Colloidal transport and flocculation are the cause of the hyperenrichment of gold in nature. PNAS 118.
Mei, Y., Sherman, D.M., Liu, W.H., Brugger, J., 2013. Complexation of gold in S3–rich hydrothermal fluids: Evidence from ab-initio molecular dynamics simulations. Chem. Geol. 347, 34–42.
Mernagh, T., Bierlein, F., 2008. Transport and Precipitation of Gold in Phanerozoic Metamorphic Terranes from Chemical Modeling of Fluid-Rock Interaction. Econ. Geol. 103, 1613–1640.
Micklethwaite, S., Cox, S.F., 2006. Progressive fault triggering and fluid flow in aftershock domains: Examples from mineralized Archaean fault systems. Earth Planet. Sci. Lett. 250, 318–330.
Mikucki, E.J., 1998. Hydrothermal transport and depositional processes in Archean lode-gold systems: A review. Ore Geol. Rev. 13, 307–321.
Miller, S.A., Collettini, C., Chiaraluce, L., Cocco, M., Barchi, M., Kaus, B.J.P., 2004. Aftershocks driven by a highpressure CO_2 source at depth. Nature 427, 724–727.
Miron, G.D., Wagner, T., Kulik, D.A., Heinrich, C.A., 2016. Internally consistent thermodynamic data for aqueous species in the system Na–K–Al–Si–O–H–Cl. Geochim. Cosmochim. Acta 187, 41–78.
Oelkers, E.H., Helgeson, H.C., 1990. Triple-ion anions and polyuuclear complexing in supercritical electrolyte solutions. Geochim. Cosmochim. Acta 54, 727–738.
Patten, C.G.C., Pitcairn, I.K., Molnár, F., Kolb, J., Beaudoin, G., Guilmette, C., Peillod, A., 2020. Gold mobilization during metamorphic devolatilization of Archean and Paleoproterozoic metavolcanic rocks. Geology 48, 1110–1114.
Petrella, L., Thébaud, N., Fougerouse, D., Evans, K., Quadir, Z., Laflamme, C., 2020. Colloidal gold transport: a key to high-grade gold mineralization? Miner. Deposita 55, 1247–1254.
Petrella, L., Thébaud, N., Evans, K., Laflamme, C., Occhipinti, S., 2021. The role of competitive fluid-rock interaction processes in the formation of high-grade gold deposits. Geochim. Cosmochim. Acta 313, 38–54.
Phillips, G.N., Powell, R., 2010. Formation of gold deposits: a metamorphic devolatilization model. J. Metam. Geol. 28, 689–718.
Plyasunov, A.V., Shock, E.L., 2001. Correlation strategy for determining the parameters of the revised Helgeson-Kirkham-Flowers model for aqueous nonelectrolytes. Geochim. Cosmochim. Acta 65, 3879–3900.
Pokrovski, G.S., Akinfiev, N.N., Borisova, A.Y., Zotov, A.V., Kouzmanov, K., 2014. Gold speciation and transport in geological fluids: insights from experiments and physical-chemical modelling. Geol. Soc. Spec. Publ. 402, 9–70.
Pokrovski, G.S., Dubessy, J., 2015. Stability and abundance of the trisulfur radical ion S3- in hydrothermal fluids. Earth Planet. Sci. Lett. 411, 298–309.
Pokrovski, G.S., Kokh, M.A., Guillaume, D., Borisova, A.Y., Gisquet, P., Hazemann, J.-L.-F., Lahera, E., Net, W.D., Proux, O., Testemale, D., Haigis, V., Jonchière, R., Seitsonen, A.P., Ferlat, G., Vuilleumier, R., Saitta, A.M., Boiron, M.-C., Dubessy, J., 2015. Sulfur radical species form gold deposits on Earth. PNAS 112, 13484–13489.
Qiu, K.F., Deng, J., Laflamme, C., Long, Z.Y., Wan, R.Q., Moynier, F., Yu, H.C., Zhang, J. Y., Ding, Z.J., Goldfarb, R., 2023. Giant Mesozoic gold ores derived from subducted oceanic slab and overlying sediments. Geochim. Cosmochim. Acta 343, 133–141.
Rauchenstein-Martinek, K., Wagner, T., Wälle, M., Heinrich, C.A., 2014. Gold concentrations in metamorphic fluids: A LA-ICPMS study of fluid inclusions from the Alpine orogenic belt. Chem. Geol. 385, 70–83.
Reed, M., Rusk, B., Palandri, J., 2013. The Butte Magmatic-Hydrothermal System: One Fluid Yields All Alteration and Veins. Econ. Geol. 108, 1379–1396.
Saunders, E.J., Pearson, N.J., O'Reilly, S.Y., Griffin, W.L., 2018. Gold in the mantle: A global assessment of abundance and redistribution processes. Lithos 322, 376–391.
Saunders, J.A., Schoenly, P.A., 1995. Boiling, collid nucleation and aggregation, and the genesis of bonanza Au-Ag ores of the Sleeper deposit. Nevada. Miner. Deposita 30, 199–210.
Shock, E.L., Helgeson, H.C., 1988. Calculation of the thermodynamic and transport properties of aqueous species at high pressures and temperatures: Correlation algorithms for ionic species and equation of state predictions to 5 kb and 1000 °C. Geochim. Cosmochim. Acta 52, 2009–2036.
Shock, E.L., Helgeson, H.C., Sverjensky, D.A., 1989. Calculation of the thermodynamic and transport properties of aqueous species at high pressures and temperatures: Standard partial molal properties of inorganic neutral species. Geochim. Cosmochim. Acta 53, 2157–2183.

Simon, A.C., Pettke, T., Candela, P.A., Piccoli, P.M., Heinrich, C.A., 2007. The partitioning behavior of As and Au in S-free and S-bearing magmatic assemblages. Geochim. Cosmochim. Acta 71, 1764–1782.
Song, M.C., Cui, S.X., Zhou, M.L., Jiang, H.L., Yuan, W.H., Wei, X.F., Lv, G.X., 2010. The Deep Oversize Gold Deposit in the Jiaojia Field, Shandong Province and Its Enlightenment for the Jiaojia-type Gold Deposits. Acta Geological Sinica 84, 1350–1358. In Chinese with English abstract.
Song, M.C., Song, Y.X., Cui, S.X., Jiang, H.L., Yuan, W.H., Wang, H.J., 2011. Characteristic comparison between shallow and deep-seated gold ore bodies in Jiaojia superlarge gold deposit, northwestern Shandong peninsula. Mineral Deposits 30, 924–932. In Chinese with English abstract.
Song, M.C., Deng, J., Yi, P.H., Yang, L.Q., Cui, S.X., Xu, J.X., Zhou, M.L., Huang, T.L., Song, G.Z., Song, Y.X., 2014. The Kiloton Class Jiaojia Gold Deposit in Eastern Shandong Province and Its Genesis. Acta Geological Sinica 88, 801–824.
Song, G.Z., Yan, C.M., Cao, J., Guo, Z.F., Bao, Z.Y., Liu, G.D., Li, S., Fan, J.M., Liu, C.J., 2017. Breakthrough and Significance of Exploration at Depth More than 1000 m in Jiaojia Metallogenic Belt, Jiaodong: A Case of Shaling Mining Area. Gold Science and Technology 25, 19–27. In Chinese with English abstract.
Stefánsson, A., Seward, T.M., 2004. Gold(I) complexing in aqueous sulphide solutions to 500 °C at 500 bar. Geochim. Cosmochim. Acta 68, 4121–4143.
Tanger IV, J.C., Helgeson, H.C., 1988. Calculation of the thermodynamic and transport properties of aqueous species at high pressures and temperatures: Revised equations of state for the standard partial molal properties of ions and electrolytes. Am. J. Sci. 288, 19–98.
Tomkins, A.G., 2013. On the sourc e of orogenic gold. Geology 41, 1255–1256.
Ulrich, T., Günther, D., Heinrich, C.A., 1999. Gold concentrations of magmatic brines and the metal budget of porphyry copper deposits. Nature 399, 676–679.
Wagner, T., Kulik, D.A., Hingerl, F.F., Dmytrieva, S.V., 2012. Gem-selektor geochemical modeling package: TSolMod library and data interface for multicomponent phase models. Can. Mineral. 50, 1173–1195.
Wang, Z.C., Cheng, H., Zong, K.Q., Geng, X.L., Liu, Y.S., Yang, J.H., Wu, F.Y., Becker, H., Foley, S., Wang, C.Y., 2020. Metasomatized lithospheric mantle for Mesozoic giant gold deposits in the North China craton. Geology 48, 1–5.
Wang, H., Lan, T.G., Fan, H.R., Huang, Z.L., Hu, H.L., Chen, Y.H., Tang, Y.W., Li, J., 2022b. Fluid origin and critical ore-forming processes for the giant gold mineralization in the Jiaodong Peninsula, China: Constraints from in situ elemental and oxygen isotopic compositions of quartz and LA–ICP–MS analysis of fluid inclusions. Chem. Geol. 608, 121027.
Wang, X., Wang, Z.C., Cheng, H., Zong, K.Q., Wang, C.Y., Ma, L., Cai, Y.C., Foley, S., Hu, Z.C., 2022a. Gold endowment of the metasomatized lithospheric mantle for giant gold deposits: Insights from lamprophyre dykes. Geochim. Cosmochim. Acta 316, 21–40.
Wang, S.R., Yang, L.Q., Kong, P.F., 2016. Permeability structure and gold deposits cluster mechanism along the Jiaojia fault, China: Structure stress transfer modeling. Acta Petrol. Sin. 32, 2494–2508. In Chinese with English abstract.
Weatherley, D.K., Henley, R.W., 2013. Flash vaporization during earthquakes evidenced by gold deposits. Nat. Geosci. 6, 294–298.
Wei, Y.J., Yang, L.Q., Feng, j.Q., Wang, H., Lv, G.Y., Li, W.C., Liu, S.G., 2019. Ore-Fluid Evolution of the Sizhuang Orogenic Gold Deposit, Jiaodong Peninsula, China. Minerals 9, 190.
Wei, Q., Fan, H.R., Lan, T.G., Liu, X., Jiang, X.H., Wen, B.J., 2015. Genesis of Sizhuang gold deposit, Jiaodong Peninsula: Evidences from fluid inclusion and quartz solubility modeling. Acta Petrol. Sin. 31, 1049–1062. In Chinese with English abstract.
Wen, B.J., Fan, H.R., Hu, F.F., Liu, X., Yang, K.F., Sun, Z.F., Sun, Z.F., 2016. Fluid evolution and ore genesis of the giant Sanshandao gold deposit, Jiaodong gold province, China: Constrains from geology, fluid inclusions and H-O–S–He–Ar isotopic compositions. J. Geochem. Explor. 171, 96–112.
Williams-Jones, A.E., Bowell, R.J., Migdisov, A.A., 2009. Gold in Solution. Elements 5, 281–287.
Wu, F.Y., Yang, J.H., Xu, Y.G., Wilde, S.A., Walker, R.J., 2019. Destruction of the North China Craton in the Mesozoic. Annu. Rev. Earth Planet. Sci. 47, 173–195.
Xia, Q.K., Liu, J., Liu, S.C., Kovacs, I., Feng, M., Dang, L., 2013. High water content in Mesozoic primitive basalts of the North China Craton and implications on the destruction of cratonic mantle lithosphere. Earth Planet. Sci. Lett. 361, 85–97.
Xu, W.G., Fan, H.R., Yang, K.F., Hu, F.F., Cai, Y.C., Wen, B.J., 2016. Exhaustive gold mineralizing processes of the Sanshandao gold deposit, Jiaodong Peninsula, eastern China: Displayed by hydrothermal alteration modeling. J. Asian Earth Sci. 129, 152–169.
Yang, L.Q., Deng, J., Wang, Z.L., Guo, L.N., Li, R.H., Groves, D.I., Danyushevsky, L.V., Zhang, C., Zheng, X.L., Zhao, H., 2016. Relationships Between Gold and Pyrite at the Xincheng Gold Deposit, Jiaodong Peninsula, China: Implications for Gold Source and Deposition in a Brittle Epizonal Environment. Econ. Geol. 111, 105–126.
Yang, K.F., Fan, H.R., Santosh, M., Hu, F.F., Wilde, S.A., Lan, T.G., Lu, L.N., Liu, Y.S., 2012. Reactivation of the Archean lower crust: Implications for zircon geochronology, elemental and Sr–Nd–Hf isotopic geochemistry of late Mesozoic granitoids from northwestern Jiaodong Terrane, the North China Craton. Lithos 146–147, 112–127.
Yang, L.Q., Guo, L.N., Wang, Z.L., Zhao, R.X., Song, M.C., Zheng, X.L., 2017. Timing and mechanism of gold mineralization at the Wang'ershan gold deposit, Jiaodong Peninsula, eastern China. Ore Geol. Rev. 88, 491–510.
Yang, Q.Y., Santosh, M., Shen, J.F., Li, S.R., 2014. Juvenile vs. recycled crust in NE China: Zircon U-Pb geochronology, Hf isotope and an integrated model for Mesozoic gold mineralization in the Jiaodong Peninsula. Gondw. Res. 25, 1445–1468.
Yang, C.X., Santosh, M., 2019. Ancient deep roots for Mesozoic world-class gold deposits in the north China craton: An integrated genetic perspective. Geosci. Front. 11, 203–214.
Yu, X.F., Yang, D.P., Li, D.P., Shan, W., Xiong, Y.X., Chi, N.J., Liu, P.R., Yu, L.H., 2019. Mineralization characteristics and geological significance in 3000 m depth of Jiaojia gold metallogenic belt. Jiaodong Peninsula. Acta Petrol. Sin. 35, 2893–2910. In Chinese with English abstract.
Zhai, M.G., Santosh, M., 2011. The early Precambrian odyssey of the North China Craton: A synoptic overview. Gondw. Res. 20, 6–25.
Zhang, L., Weinberg, R.F., Yang, L.Q., Groves, D.I., Sai, S.X., Matchan, E., Phillips, D., Kohn, B.P., Miggins, D.P., Liu, Y., Deng, J., 2020. Mesozoic Orogenic Gold Mineralization in the Jiaodong Peninsula, China: A Focused Event at 120±2 Ma During Cooling of Pregold Granite Intrusions. Econ. Geol. 115, 415–441.
Zhang, B.L., Yang, L.Q., Huang, S.Y., Liu, W.L., Zhao, R.X., Xu, Y.B., Liu, S.G., 2014. Hydrothermal alteration in the Jiaojia gold deposit, Jiaodong. China. Acta Petrol. Sin. 30, 2533–2545. In Chinese with English abstract.
Zheng, Y.F., Fu, B., Gong, B., Li, L., 2003. Stable isotope geochemistry of ultrahigh pressure metamorphic rocks from the Dabie-Sulu orogen in China: implications for geodynamics and fluid regime. Earth Sci. Rev. 62, 105–161.
Zhu, Y.F., An, F., Tan, J.J., 2011. Geochemistry of hydrothermal gold deposits: A review. Geosci. Front. 2, 367–374.
Zhu, R.X., Fan, H.R., Li, J.W., Meng, Q.R., Li, S.R., Zeng, Q.D., 2015. Decratonic gold deposits. Sci. China Earth Sci. 58, 1523–1537.
Zhu, D.C., Zhang, W., Wang, Y.P., Tian, J.X., Liu, H.D., Hou, J.H., Gao, H.L., 2018. Characteristics of Ore Bodies and Prospecting Potential of Zhaoxian Gold Deposit in Laizhou City of Shandong Province. Shandong Land and Resources 34, 14–19. In Chinese with English abstract.